



Full length article

Characteristics and evolution of the late Permian “source-to-sink” system of the Beisantai area in the eastern Junggar Basin, NW China

Qisong Xu^{a,b}, Jian Wang^{a,b,c,*}, Yingchang Cao^{a,b,c}, Xintong Wang^{a,b}, Jie Xiao^{a,b}, Kashif Muhammad^{a,b}

^a School of Geosciences, China University of Petroleum (East China), Qingdao 266580, China

^b Petroleum Reservoir Institute, China University of Petroleum (East China), Qingdao 266580, China

^c Laboratory for Marine Mineral Resources, Qingdao National Laboratory for Marine Science and Technology, Qingdao 266071, China

ARTICLE INFO

Keywords:

“Source-to-sink” system

Sediment routing

Source area

Sediment discharge

Sedimentary evolution

Eastern Junggar Basin

ABSTRACT

Many studies have focused on the tectonic evolution and sedimentary processes of the Beisantai Uplift, NW China during the late Permian. However, the sedimentary characteristics of the area are still not well documented due to a complex tectonic evolution of the uplift and the limited distribution of core data. To understand the sedimentary evolution of this study area, a “source-to-sink” system research is adopted. First, the research redefines the sequence stratigraphic framework of the late Permian, which corresponds to a complete third-order sequence that can be further divided into a transgressive system tract (TST) and a regressive system tract (RST). Then, the integration of three-dimensional (3D) seismic reflection data, well logs, mud logs and core data provides new insights into the transportation and sedimentary processes within the “source-to-sink” system. The different characteristics of the source area, transfer system and sedimentary paleogeomorphology between the TST stage and RST stage ultimately led to significantly different sedimentary characteristics in the two stages.

In the TST stage, the “source-to-sink” system exhibited a continued transgressive depositional characteristic that matched the sediment discharge evolution. The steeper sedimentary paleogeomorphology enabled the development of large-scale fan deltas with few beach bars. During the RST stage, the “source-to-sink” system had low sediment discharge and a smooth sedimentary paleogeomorphology. The “source-to-sink” system was predominantly characterized by small-scale beach bars with few fan deltas. With the decreasing level of sediment discharge and continued smoothing of the sedimentary paleogeomorphology, the beach bars expanded.

1. Introduction

The Earth's surface can be divided into denudational and sedimentary geomorphic domains according to their origins. A “source-to-sink” system refers to the entirety of sediments produced from the source, moved via transport, and finally deposited in the sink. In the late 1990s, the MARGINS Program started a new chapter of “source-to-sink” system research. Many “source-to-sink” system research projects were initiated, including the “InterMargins”, “EuroSTRATAFORM” and “Asian Delta: evolution and modern change”. These projects promoted “source-to-sink” system studies (Margins Program, Science Plans 2004, 2003; Weaver et al., 2006; Zhu et al., 2017). To date, “source-to-sink” system analysis has become an effective method for revealing the filling process of sedimentary basins and predicting sedimentary bodies. During the process of analysis, numerous studies have developed sufficient methods and obtained a better understanding to reveal different

aspects of “source-to-sink” systems. For example, a wealth of studies have attempted to quantify sediment discharge variations in source areas to predict downstream system responses (Allen et al., 2013; Armitage et al., 2011; Holbrook and Wanas, 2014; Lin and Bhattacharya, 2017; Sharma et al., 2017; Sømme et al., 2011; Xu et al., 2017; Zhang et al., 2016). Moreover, researchers have identified “source-to-sink” systems and constrained deposition behaviors by analyzing transport passageways and processes (Blum et al., 2013; Garzanti, 2017; Johnsson, 1993; Romans et al., 2016). However, studying ancient “source-to-sink” systems is still challenging because of the shortage of stratigraphic records and their subsequent diagenesis or deformation. In addition, little work has been done on continental basins in compressional settings. In fact, sediment accumulations in the basin indirectly reflects the combined effects of the external perturbations and internal responses of different segments, including tectonic and climate perturbations, source area evolution and its sediment

* Corresponding author.

E-mail address: wangjian8601@163.com (J. Wang).

<https://doi.org/10.1016/j.jseaes.2019.103907>

Received 23 September 2018; Received in revised form 20 June 2019; Accepted 25 June 2019

Available online 26 June 2019

1367-9120/ © 2019 Elsevier Ltd. All rights reserved.

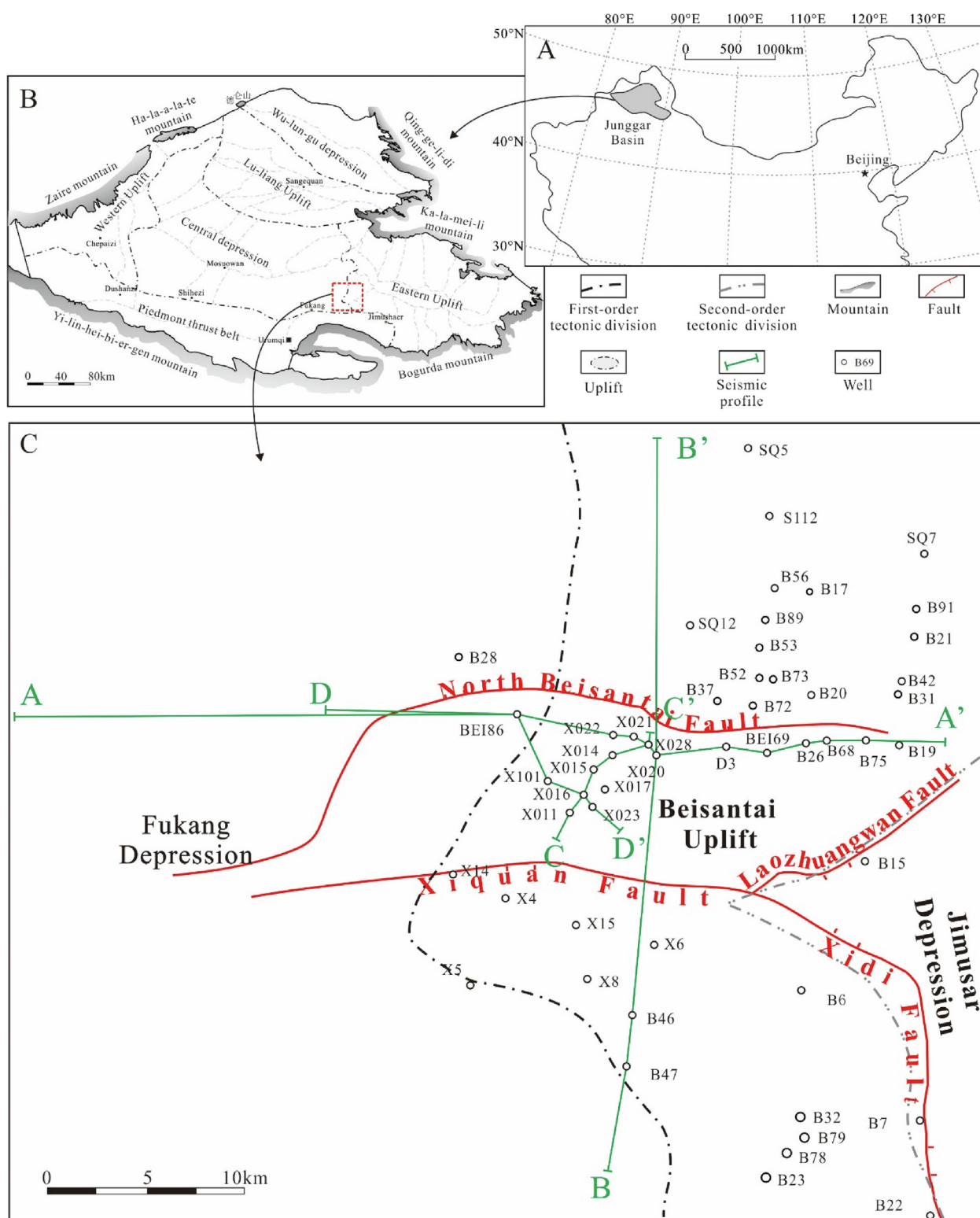


Fig. 1. (A) Map of North China showing the location of the Junggar Basin. (B) Tectonic map of the Junggar Basin showing the location of the research area in the eastern Junggar Basin. (C) Tectonic setting of the research area with locations of the seismic lines shown in green. (For interpretation of the references to colour in this figure legend, the reader is referred to the web version of this article.)

discharge responses, transport responses, and paleogeomorphologic responses (Dong et al., 2016; Schattner and Lazar, 2016). Therefore, the whole “source-to-sink” system can be reconstructed through the analysis of different segments with the consideration of tectonic and climate perturbations.

The Beisantai Uplift is located in the eastern Junggar Basin, NW

China (Fig. 1A, B). In the late Permian, the area around the uplift (called the Beisantai area hereafter) was dominated by sand-rich sediments supplied from the uplift, forming an important hydrocarbon-rich unit in the Junggar Basin (Xu et al., 2016; Zhang, 2011). Due to the special position of the Beisantai area during hydrocarbon exploration (similar to the forebulge area of the North Alpine Foreland Basin), many

studies have focused on the tectonics and sedimentology of the area (Chen et al., 2001; Crampton and Allen, 1995; Li et al., 2005, 2016; Wang et al., 2016; Wu et al., 2005, 2004; Xiao, 2015; Xu et al., 2016; Zhang, 2011). However, a limited distribution of core data and multiple stages of subsequent deformation have hindered geological research on the Permian system, especially in sedimentology. The sediment routing and depositional behaviors are still highly controversial (Deng et al., 2011; Ren et al., 2016; Wang et al., 2016; Xu et al., 2016; Zhang, 2011). Accordingly, a comprehensive study of the “source-to-sink” system within the context of tectonic and climate perturbations is applied to reveal the sediment routing and sedimentary evolution around the Beisantai Uplift. Furthermore, the “source-to-sink” system of this region will provide a better understanding of the ancient “source-to-sink” systems in continental basins.

2. Geological setting and previous work

2.1. Regional tectonics

The Beisantai area has always been treated as one part of the foreland basin system in the eastern Junggar Basin (Chen et al., 2001). The orogenesis of the Bogda Mountain shaped the tectonic framework and led to the concentrated stress in the Beisantai area (Li et al., 2016; Wu et al., 2004). The Beisantai Uplift developed with a core composed of a Carboniferous paleo-uplift in the eastern part of the area. The development of the North Beisantai and Xiquan Faults affected the evolution of the Beisantai Uplift (Fig. 1B). To the west and south of the uplift, two slopes connected the uplift and the Fukang Depression (Fig. 1B) (Wu et al., 2004). However, the tectonic setting of the Beisantai area is still in doubt due to uncertainty about the orogenesis of Bogda Mountain. Concerning the late Permian, debates have focused on whether the Beisantai area was a part of the foreland basin formed by the orogenesis of Bogda Mountain (Cai et al., 2000; Fang et al., 2006; Liu et al., 1994; Shu et al., 2005; Wang, 2003; Wu et al., 2004, 2005). Recent researches have indicated that Bogda Mountain was initially uplifted during the late Permian (Li et al., 2016; Wang et al., 2016, 2018). Meanwhile, the Beisantai area began to become part of foreland basin system (Li et al., 2016). As the research area evolved into a weak intracontinental compressional stage in the Early Triassic from the intracontinental compressional stage in the late Permian, the tectonic activity can be inferred to have continuously weakened during the late Permian (Fig. 2) (Wang et al., 2016; Wu et al., 2012). The tectonic evolution of the Beisantai area can be described based on the foreland evolution model and seismic reflection termination (Wang et al., 2016, 2018; Yang, 2011; Yang and Miall, 2010). In the early late Permian, high tectonic strength cause basement subsidence, and then onlaps develop (Fig. 3). Subsequently, the tectonic strength decreased during the early late Permian, leading to the weakening basement subsidence (Fig. 2). Until the end of the late Permian, the research area entered the tectonic activity quiescent period with the basement rebounding (Fig. 2) (Yang, 2011; Yang and Miall, 2010), which led to the development of truncations on the uplift (Fig. 3).

2.2. Climate

The climate was dominantly humid to subhumid during the late Permian (Thomas et al., 2011; Yang et al., 2010). The climate evolution is shown in Fig. 2. In the early part of the late Permian, the climate was transformed into a subhumid and humid climate from the semiarid conditions at the end of the middle Permian (Wu, 1998, 1996; Yang et al., 2010). At the beginning of the late Permian, the climate was slightly drier than later (Thomas et al., 2011). Then, the humidity continued to increase with sufficient precipitation and warm temperatures (Thomas et al., 2011). In the latter part of the late Permian, the climate had changed from a generally stable humid climate to a drier and slightly subhumid climate (Thomas et al., 2011). Subsequently, the

aridity continued to increase and the climate finally evolved into the subhumid to semiarid conditions at the end of the late Permian (Thomas et al., 2011; Wu, 1996; Yang et al., 2010).

2.3. Sequence stratigraphy

Sequence stratigraphic analyses in the Beisantai and adjacent areas have shown two possible sequence stratigraphic frameworks for the late Permian (Li et al., 2005; Xiao, 2015; Zhang, 2011). One study purposed that the late Permian developed one third-order sequence (Zhang, 2011), whereas other studies suggested that the late Permian could be divided into two third-order sequences (Li et al., 2005; Xiao, 2015). As the previous sequence stratigraphic framework is still controversial, this paper used seismic reflection terminations, stacking patterns and sedimentary petrology to redefine the sequence stratigraphic framework of the late Permian (Figs. 2 and 3). The late Permian is comprised by the Wutonggou Formation, which corresponds to a third-order sequence (SQP_{3wt}) based on the identification of the sequence boundaries. Both the upper and lower sequence boundaries are characterized by truncated and onlap seismic reflections on the seismic profile (Fig. 3). The abrupt changes of sedimentary petrology and stacking patterns also confirm the upper and lower sequence boundaries. Across the lower sequence boundary of the SQP_{3wt}, fine-grained deposits with a progradation stacking pattern change to sandy conglomerates with a retrogradation stacking pattern (Fig. 2). Across the upper sequence boundary of the SQP_{3wt}, the deposits become coarser and the stacking pattern changes from progradation to aggradation (Fig. 2).

The sequence structure of the SQP_{3wt} was also investigated to discuss the evolution of the “source-to-sink” system in the different periods of the SQP_{3wt}. As previous studies suggested, the sequence of the intracontinental compressional basin presents dual features (Jiang et al., 2009; Zhu et al., 2018). The SQP_{3wt} is divided into a transgressive system tract (TST) and a regressive system tract (RST) bounded by the maximum flooding surface (MFS) (Jiang et al., 2009; Zhu et al., 2018). Compared with previous studies, both the tectonic and climatic evolution are considered here as a part of the sequence architecture analysis. In the early late Permian, subsidence caused by the strong tectonic activity and wet climate caused the base level to rise (Fig. 2). The TST stage developed with onlap seismic reflections and a retrogradation stacking pattern (Figs. 2 and 3). At the end of the late Permian, the rebounding of the basement during the tectonic activity quiescent period and dry climate caused the base level to fall, leading to the truncation seismic reflections and progradation stacking pattern during the RST stage (Figs. 2 and 3).

3. Methods and database

This research was based primarily on three-dimensional seismic data and geological data from 43 exploration wells that contain well logs, mud logs and core data (13 wells). The three-dimensional seismic dataset covered an area of approximately 1900 km² and was interpreted in a grid of 30 × 30 using the Landmark OpenWorks software version 5000 (see the 3D seismic data in Fig. 13).

The paleogeomorphology provides the foundation for the “source-to-sink” system analysis. Both the macroscopic paleogeomorphologic patterns and meticulous depictions of geomorphic units were applied in this research. The macroscopic paleogeomorphologic patterns were reconstructed by the impression method (Feng et al., 2015; Jin et al., 2017). The MFS was selected as the top surface for calculating the impression seismic thickness of the TST stage, since it is more easily traced and has filling characteristics. For the RST stage, the upper boundary of SQP_{3wt} was selected because of its weak erosion. Then, we used the horizon calculation module in Landmark to calculate and interpolate the time domain thicknesses of the TST stage and the RST stage. Subsequently, the time domain thickness data was displayed in a 3D viewer using Petrel software. Because of the regional compaction

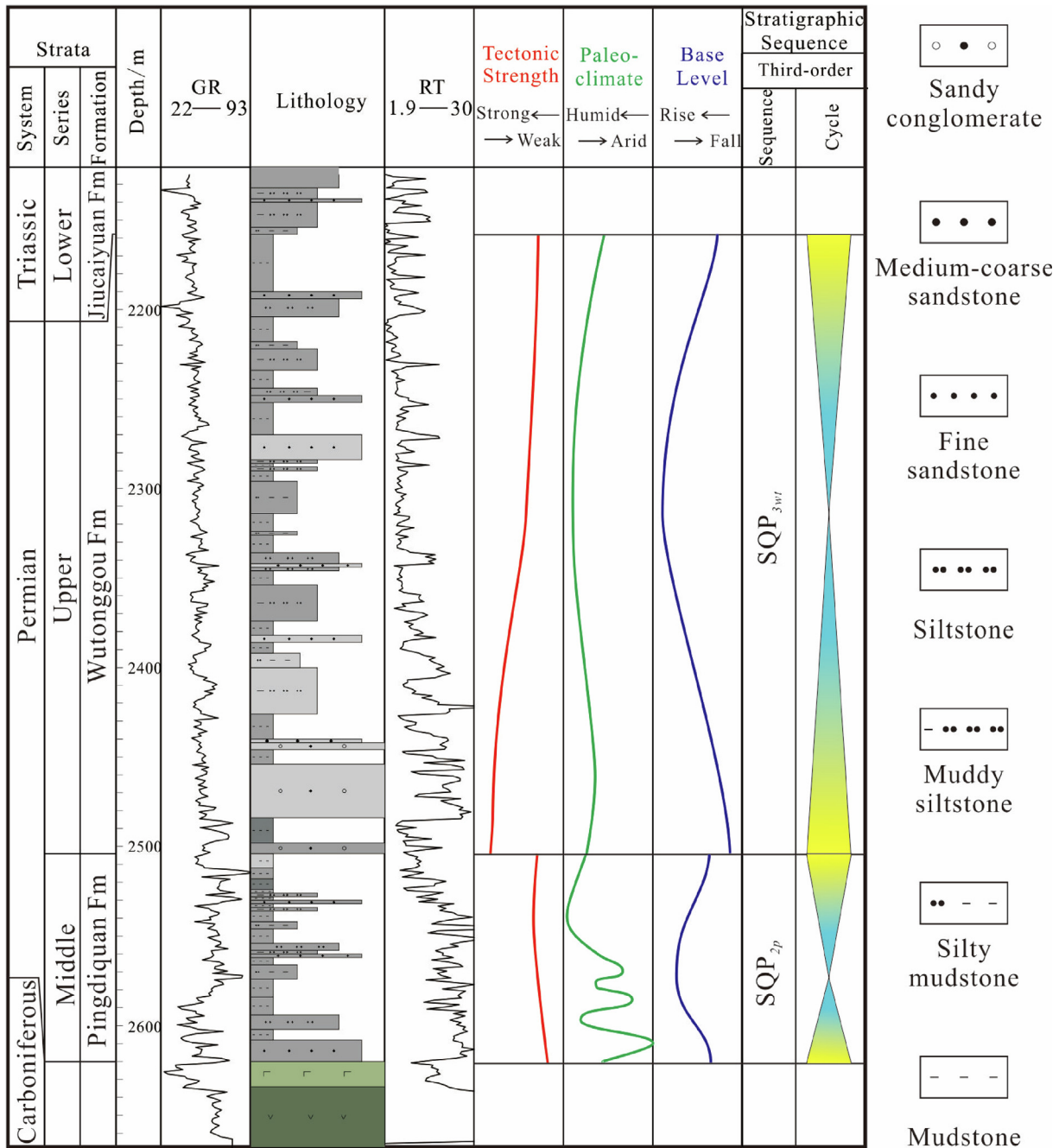


Fig. 2. Synthetic columns showing the Permian sequence stratigraphy, tectonics and climate in the study area. Tectonic and climatic evolution interpretations are derived from previous studies (Wang et al., 2016; Li et al., 2016; Wang et al., 2018, Wu, 1996; Wu, 1998; Yang et al., 2010; Thomas et al., 2011).

and long-term sedimentation, compaction didn't change the macroscopic paleogeomorphic patterns and the ancient water depth weakly influenced the thickness. Therefore, compaction and ancient water depth correction were not applied (Xian et al., 2017).

The meticulous depictions of the geomorphic units focused on the source area and valley. Every onlap and truncation point were traced and mapped in planar view to show the spatial distribution of the source area. Then, we used the distance/area module in Landmark to estimate the size of the source area. Based on the source area distribution and size, the evolution of the source area was reconstructed with the base level changes indicated by the tectonic and climatic evolution.

The valleys were recognized through seismic reflection terminations and sedimentologic analysis of well logs, mud logs and cores (Bridge

and Tye, 2000; Plint and Wadsworth, 2003; Reijenstein et al., 2011; Zhu et al., 2012). Then, the geometry of the valleys could be measured directly from the core data (for example, measurements of the valley story thickness and grain size) or estimated from empirical equations (for example, measurements of the valley width and paleoslope, W_v and S , respectively) (Bridge and Tye, 2000; Holbrook and Wanas, 2014; Leopold and Maddock, 1953). The full story thickness of the valleys can be used as a direct proxy for the average bankfull depth (H_{bf}), which is half of the valley story thickness (Sharma et al., 2017). In this research, two complete successions and two incomplete successions of one well were measured as the maximum and minimum story thicknesses to calculate the average bankfull depth (H_{bf}) and its average value. Although few valley data were available, the maximum, minimum and average values of the average bankfull depth (H_{bf}) can reduce the errors

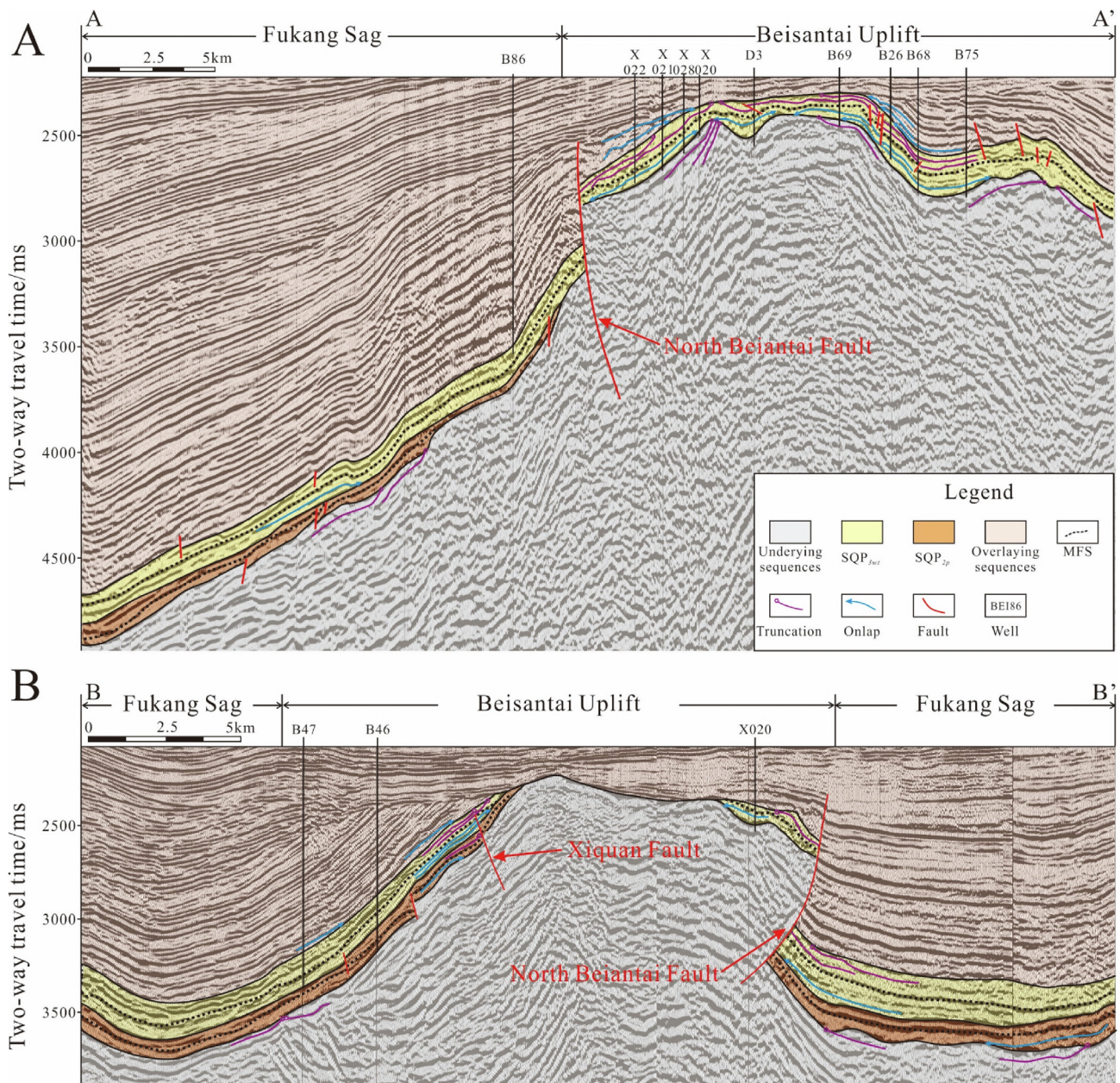


Fig. 3. Seismic reflection characteristics and sequence stratigraphic distribution in the (A) S-N direction and (B) E-W direction.

and reflect the change of average bankfull depth (H_{bf}) (Lin and Bhattacharya, 2017). The bankfull valley width (W_v) can be measured from the seismic data. However, the measured width represents the width of the multistory valley because of the insufficient resolution of seismic data. Therefore, the bankfull valley width (W_v) is approximated from empirical equations based on the assumption of a single-thread (Eq. (1); Bridge and Tye, 2000; Holbrook and Wanas, 2014) or fully braided valley (Eq. (2); Leopold and Maddock, 1953; Holbrook and Wanas, 2014). Although the types of valleys are not recognized, the average value ($W_{v-average}$) of the bankfull valley width (W_v) from two empirical equations can help reduce the errors.

$$W_v = 8.8H_{bf}^{1.82} \tag{1}$$

$$W_v = 42H_{bf}^{1.1} \tag{2}$$

The valley-filling epochs were divided by tracking every seismic event of the section along the valley and the stratigraphic correlations of the cross-well section along the valley. In addition, the sedimentary

characteristics of the valley-filling epochs were obtained from the mud logs, well logs and cores (if available), which were calibrated to the seismic data using the well time-depth measurements from the oil field.

The sedimentary characteristics of the “source-to-sink” system were investigated through the sedimentological and petrological analysis of well data and seismic data. These analyses also played a role in reconstructing the sediment routing system. The petrological characteristics were recognized through descriptions of cores and sections. Moreover, the sediment composition was determined from point counts of 58 thin sections from 13 wells, each of which was examined through 300 fields of view (Wang et al., 2017). The genesis of each sand body was identified by interpreting the petrological characteristics and stacking patterns of well logs and cores. The spatial and temporal patterns of sediment dispersal were mapped by a sedimentological interpretation of the well data and seismic attributes (such as the root mean square amplitude in this study) from stratal slicing (Zeng, 2010; Zeng et al., 2001).

The preserved sediment volume of every stratal slice was estimated

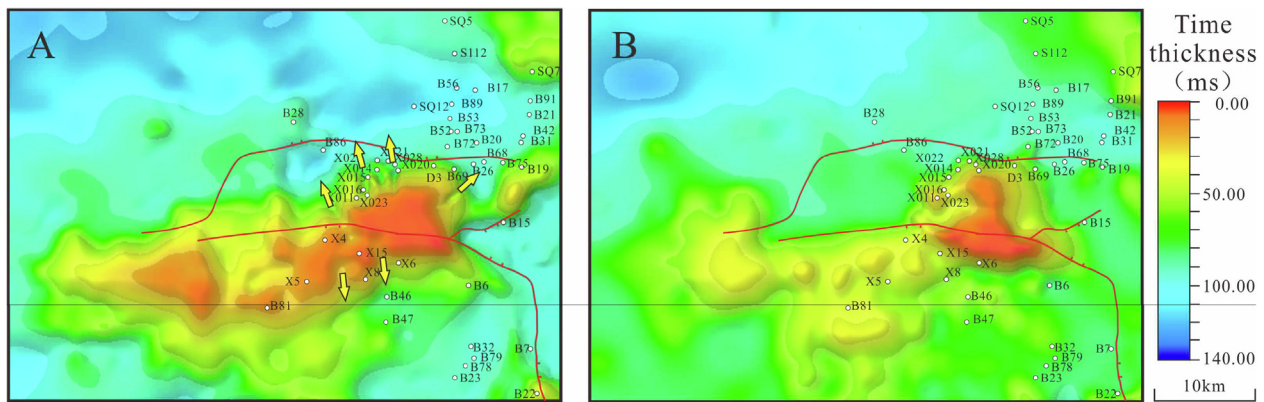


Fig. 4. Paleogeomorphology of (A) the TST stage and (B) the RST stage in the late Permian. The yellow arrows indicate the sediment supply directions from the valleys. (For interpretation of the references to colour in this figure legend, the reader is referred to the web version of this article.)

to offer a better insight into the sediment supply and system evolution. The volume calculation was completed using Petrel for each stratal slice (Carvajal and Steel, 2012; Sømme et al., 2011). First, surfaces in the time domain of stratal slices were transformed into the depth domain based on the time-depth relationship fitting from 10 wells. Then, we calculated the thickness in time of each stratal slice and gridded the thickness extrapolation to the whole research area. Finally, we calculated the grid volumes within the polygon of each sedimentary sand body (including fan deltas and beach bars). Thus, the preserved sediment volumes of the total area and each sedimentary body were calculated.

4. Results and interpretation

4.1. Paleogeomorphology

4.1.1. Macroscopic paleogeomorphologic patterns

The paleogeomorphology is quite different between the TST stage and the RST stage. In the TST stage, the Beisantai Uplift is very large and surrounded by steep topography (Fig. 4A). The slope gradients decrease from the bottom surface to the maximum flooding surface (MFS) during the TST stage (Fig. 3B). In contrast, a small uplift develops with gentle topography during the RST stage (Fig. 4B). The slope gradients remain stable from the MFS to the top surface during the RST stage (Fig. 3B). During the same period, spatial differences in the paleogeomorphology also develop. In the TST stage, the steep slopes and low topographies mainly develop in the northern and eastern areas around the uplift (Fig. 4A). The gentler slopes and lower topographies develop far away from the uplift (Fig. 4A). In the RST stage, the paleogeomorphology inherits the pattern of the TST stage, but the slopes are gentler and the topographies are higher (Fig. 4B). Steep slopes only develop in the northeastern area near the uplift (Fig. 4B). The low topographies mainly locate in the northern area (Fig. 4B). The spatial differences of gradient and relief in the different regions decreased during the RST stage (Fig. 4B).

4.1.2. Distribution and size of the Beisantai uplift

Six epochs were defined within the SQP_{3wt} by tracing every seismic phase axis (Fig. 6B), and detailed maps of the distribution and size of the Beisantai Uplift were created by tracing the onlap points of every epoch, where possible (Figs. 3 and 5). The distribution and size during each epoch represent the results at the end of the epoch and control the sedimentation of the next epoch. Epochs 1 to 3 corresponds to the TST stage, and Epochs 4 to 6 corresponds to the RST stage. During the TST stage, the sequences of Epochs 1 to 3 onlap gradually towards the uplift (Fig. 3). This feature indicates the expansion of the sedimentary range and the atrophy of the uplift (Xian et al., 2017). The size varies from 464.65 km² to 38.61 km² from Epoch 1 to Epoch 3 (Fig. 5A–C), and the

Beisantai Uplift atrophies in the north and west directions with negligible migration to the south (Fig. 5A–C). During the RST stage, the uplift expands as a whole. The size increases from 54.59 km² to 38.61 km² from Epoch 4 to Epoch 5 (Fig. 5D and E). Since the final truncation points of the SQP_{3wt} display the source area distribution of the later Epoch 5 or the beginning of Epoch 6, the source area distribution of the later Epoch 6 cannot be estimated.

4.1.3. Valley distribution, geometry and filling epoch

The valleys were recognized by cut and fill patterns of various sizes in the 3D seismic data, and then the geometry and filling of these valleys were analyzed. Valleys mainly develop in the northern part of the uplift (Fig. 4A). These valleys are often wide and relatively shallow in the seismic profiles (Fig. 6A). By tracing every epoch along the valleys, we find that most valleys develop only during the TST stage and were filled in during the Epoch 2 (Valley 1) and Epoch 3 (Valley 2) (Figs. 6 and 7). From Epoch 2 to Epoch 3, the valleys become narrow and shallow, with the bankfull valley depths (H_{bf}) falling from 4.8–1.96 m to 1.75–0.51 m and the average bankfull valley widths ($W_{v-average}$) decreasing from 77.06–24.78 m to 21.98–4.50 m. Moreover, the paleoslope becomes steeper during Epoch 3 (Figs. 6A, 7, Table 1). In Epoch 4 of the RST stage, sediments have already filled and leveled the valleys.

4.2. Petrological characteristics and interpretation of sand body genesis

4.2.1. Petrological characteristics

The sediments around the uplift are characteristically high in lithic fragments during the TST stage and RST stage (Fig. 8A). Sedimentary and igneous rock fragments dominate the composition of rock fragments in both the TST stage and the RST stage (Fig. 8B). Further investigations based on thin sections show that the sedimentary rock fragments mainly consist of mudstone (Fig. 9F) and that intermediate and mafic extrusive rocks are the main types of igneous rock fragments (Fig. 9G–I).

The grain size varies from pebbles to mud (Figs. 7, 9A–D). The pebble-rich sandstones primarily develop near the uplift during the TST stage (Fig. 9A–C). The pebbles consist mostly of mudstones and igneous rocks, are poorly sorted and had low roundness (Fig. 9A–C). The pebbles are all subrounded to subangular (Fig. 9A–C). In contrast, the fine sediments mainly develop far away from the uplift during the TST stage and in most areas during the RST stage and display good sorting and roundness (Figs. 9D, 10).

4.2.2. Interpretation of sand body genesis

The genesis of sand bodies with different sedimentary characteristics are identified from well logs, mud logs and cores. These genesis types include valley fillings, subaqueous distributary channels, mouth

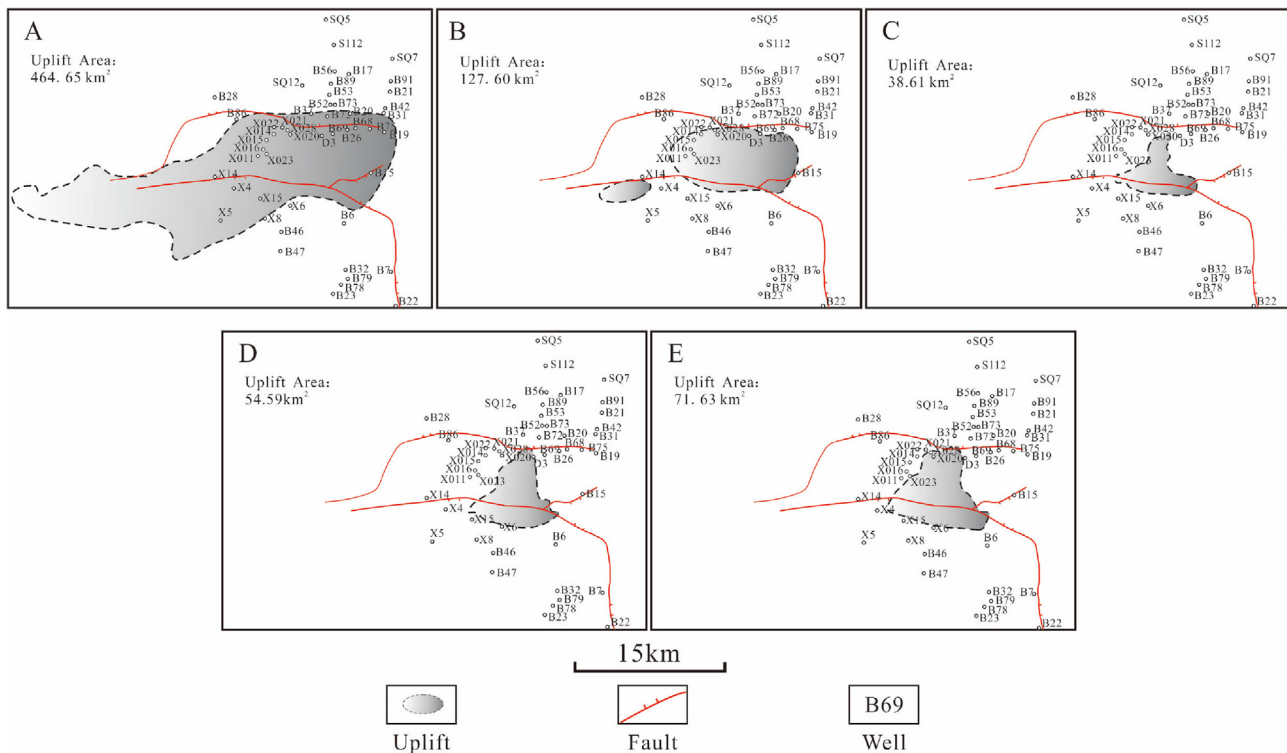


Fig. 5. The Beisantai Uplift size and distribution from Epoch 1 to Epoch 5 (A-E). Every map shows the size and distribution at the end of the epoch.

bars and sheet sands of fan deltas and beach bars. The key observations and interpretations of their sedimentary characteristics are summarized below.

(1) Valley filling

The fining-upward successions with cut and fill patterns on the uplift are interpreted as valley fillings (Figs. 6A, 7) (Bhattacharya et al., 2016; Sharma et al., 2017; Zhu et al., 2012, 2014). The rock types vary from muddy siltstone to pebbly fine sandstone (Figs. 6A, 7). The valley fillings coarsen from Epoch 2 to Epoch 3 (Figs. 6A, 7). Moreover, the deposits of each epoch have multiple episodes of cutting and filling (Fig. 7). During the RST stage, the valleys have already been filled and overlain with silty-muddy sediments (Fig. 7).

(2) Fan delta

Three types of sand bodies develop in the fan delta, including subaqueous distributary channels, mouth bars and sheet sands (Fig. 10A-B). The fining-upward successions with pebbles at the bottom, parallel bedding and cross-bedding are interpreted as subaqueous distributary channels (Jia et al., 2016; Zhang et al., 2018). The subaqueous distributary channels are mainly marked by pebbly sandstone or sandstone with different grain sizes (Figs. 9A-B, 10A). The pebbly sandstones consist of sedimentary and igneous pebbles (Fig. 9A-B) with poor sorting and roundness. The multiple erosional surfaces indicate the amalgamation of subaqueous channel deposits (Tan et al., 2018) (Fig. 10A).

The coarsening-upward cycles of silt to fine-grained sandstone are interpreted as a mouth bar deposit (Figs. 9D, 10A) (Jia et al., 2016). A few pebbles with good sorting and roundness develop at the top of an individual coarsening-upward cycle (Fig. 10A). In addition, most mouth bars directly connect to the subaqueous distributary channel with parallel bedding, cross-bedding and ripple cross-bedding (Figs. 9D, 10A).

The sheet sands mainly consist of silt to fine-grained sand with good

sorting and roundness (Fig. 10B). This type of sand body rarely develops in the form of sandstone interbeds among the mudstone or silty mudstone deposits with massive bedding (Fig. 10B). Sometimes, sheet sands also form thin coarsening-upward cycles (Fig. 10B).

(3) Beach bars

Beach bars were always divided into deposits of beaches and bars in focused studies of beach bars (Deng et al., 2011; Jiang et al., 2011; Tan et al., 2018). This study treated the beach bars as a continuous sedimentary package since their detailed characterization is not the main point of this research.

In the study area, no cores can be used to identify the beach bars. Therefore, the stacking patterns interpreted from the well logs and the lithologies from the mud logs and paleogeomorphological setting were used to identify beach bars. The coarsening-upward successions of silty mudstones and muddy siltstones are interpreted as beach bars (Fig. 10C) (Deng et al., 2011; Jiang et al., 2011; Tan et al., 2018). These bars mainly develop in the gentle region far away from the uplift (Fig. 4) (Jiang et al., 2011).

5. Discussion

5.1. Sediment routing

Based on the paleogeomorphological, petrological and seismic attributes, the sediment routing system can be reconstructed. During the SQP_{3WB} the Beisantai Uplift are exposed above the water and acts as a potential source area (Figs. 4 and 5). The valleys formed on the uplift also indicate that the uplift feed the area (Figs. 4A, 6). Additionally, the abundant rock fragments and poorly sorted, angular pebbles of the TST stage indicate that the sediments come from a nearby source area (Figs. 8A, 9A-B). In the RST stage, the abundant rock fragments also indicate the proximal deposit setting, despite the lack of pebbles (Fig. 8A). In addition, the well matching relationship between composition of rock fragments and the petrologic feature of preserved

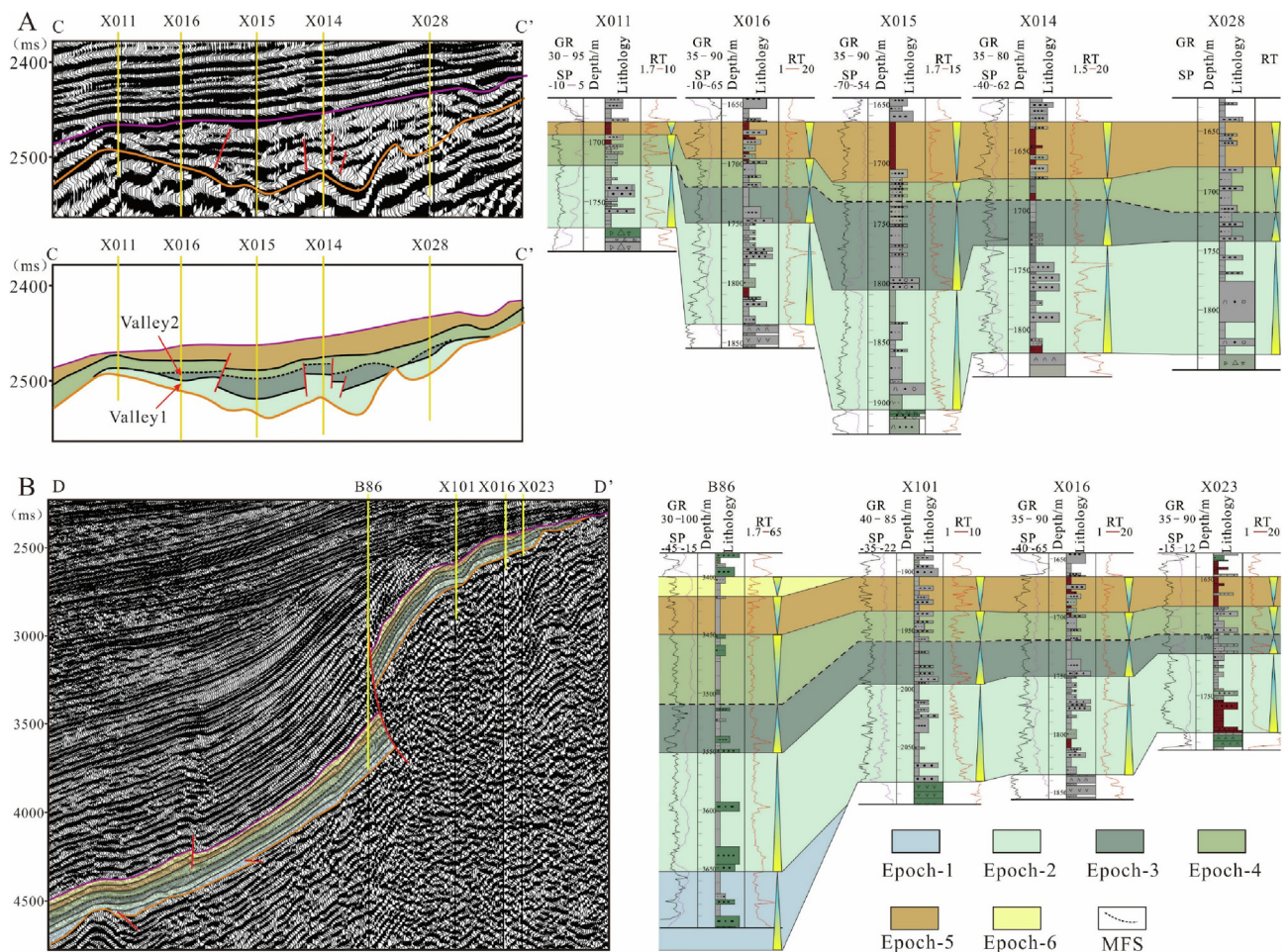


Fig. 6. (A) Valley geometry and filling characteristics. During Epochs 2–3, the valleys filled and narrowed after not filling in Epoch 1. The calibrations of valleys 1 and 2 in Fig. 7 are also shown. Valley 1 and valley 2 developed during Epoch 2 and Epoch 3, respectively. (B) The along-valley seismic and well profiles that show the epoch dividing along the valley during the late Permian. Epochs 1–3 overlapped towards the uplift.

formations on the uplift shows that the uplift feed the Beisantai area. The igneous rock fragments and pebbles are mainly derived from Carboniferous intermediate and mafic extrusive rocks in the uplift (Fig. 9J–K). The mudstones of the Pingdiquan Formation in the uplift supply the mudstone rock fragments and pebbles (Fig. 9E). In summary, the Beisantai Uplift clearly supplies the surrounding area to construct the “source-to-sink” system. Moreover, the sediment routing shows no obviously change from the TST stage to RST stage since the similarly proximal deposit settings and rock fragment types are observed (Fig. 8). The inherited development of the paleogeomorphologic patterns also proves the existence of the same sediment routing. Previous studies also reached the same conclusion (Ren et al., 2016; Xu et al., 2016).

5.2. Evolution of the source area

Source area reconstruction improves our understanding of sinks (Helland-hansen et al., 2016; Walsh et al., 2016). The source area evolution, including the source area size and relief, strongly controls the sediment discharge and downstream system evolution (Bhattacharya et al., 2016). Therefore, this paper first discusses the source area evolution after identifying the sediment routing to provide a foundation for reconstructing the “source-to-sink” system. In previous studies, the source area was treated as the thrust front uplift of Bogda Mountain. However, the source area cannot be completely described by either an elastic lithosphere flexure model or a viscoelastic lithosphere flexure model during the late Permian (Beaumont et al., 1988; Flemings and Jordan, 1990). The location of the source area is mostly constant

with decreasing size during the orogeny of Bogda Mountain (Fig. 5). The special spatial distribution also suggests that the Beisantai Uplift is not the thrust front uplift. Moreover, seismic reflection data show that the Beisantai Uplift are overlapped by the middle Permian sequence, which implies that the Beisantai Uplift is a basement uplift that developed before the late Permian (Fig. 3). In fact, the source area evolution is controlled by the integration of basement movement, differences in faulting strength, and climate change (Fig. 14). The North Beisantai Fault and Xiquan Fault are active and controlled the evolution of the source area during the late Permian (Wu et al., 2004) (Fig. 3). During the TST stage, strong faulting develops with the strong tectonic activity. The strong faulting of the North Beisantai Fault shown in the seismic profile causes the high relief and steep gradient to migrate and narrow to the north during the TST stage (Fig. 11A–C). Lower and gentler topography remain to the south of the uplift (Fig. 11A–C), and the watersheds migrate to the north. With the decreasing strength of the tectonic activity and basement subsidence, high relief and steep gradients decrease overall (Fig. 11A–C). Meanwhile, the wet climate and subsidence lift the base level to submerge the southern part of the source area since the southern part is lower (Fig. 11A–C). More areas are exposed to produce sediment in the northern source area. Similarly, the stronger faulting in the east along the North Beisantai Fault and Xiquan Fault may have resulted in the submergence of the western source area and exposure of the eastern source area to produce sediment (Fig. 5A–C). The different faulting in space finally results in the continued decreasing of the source area in the northeast direction with the migration of the high relief and steep gradient towards the

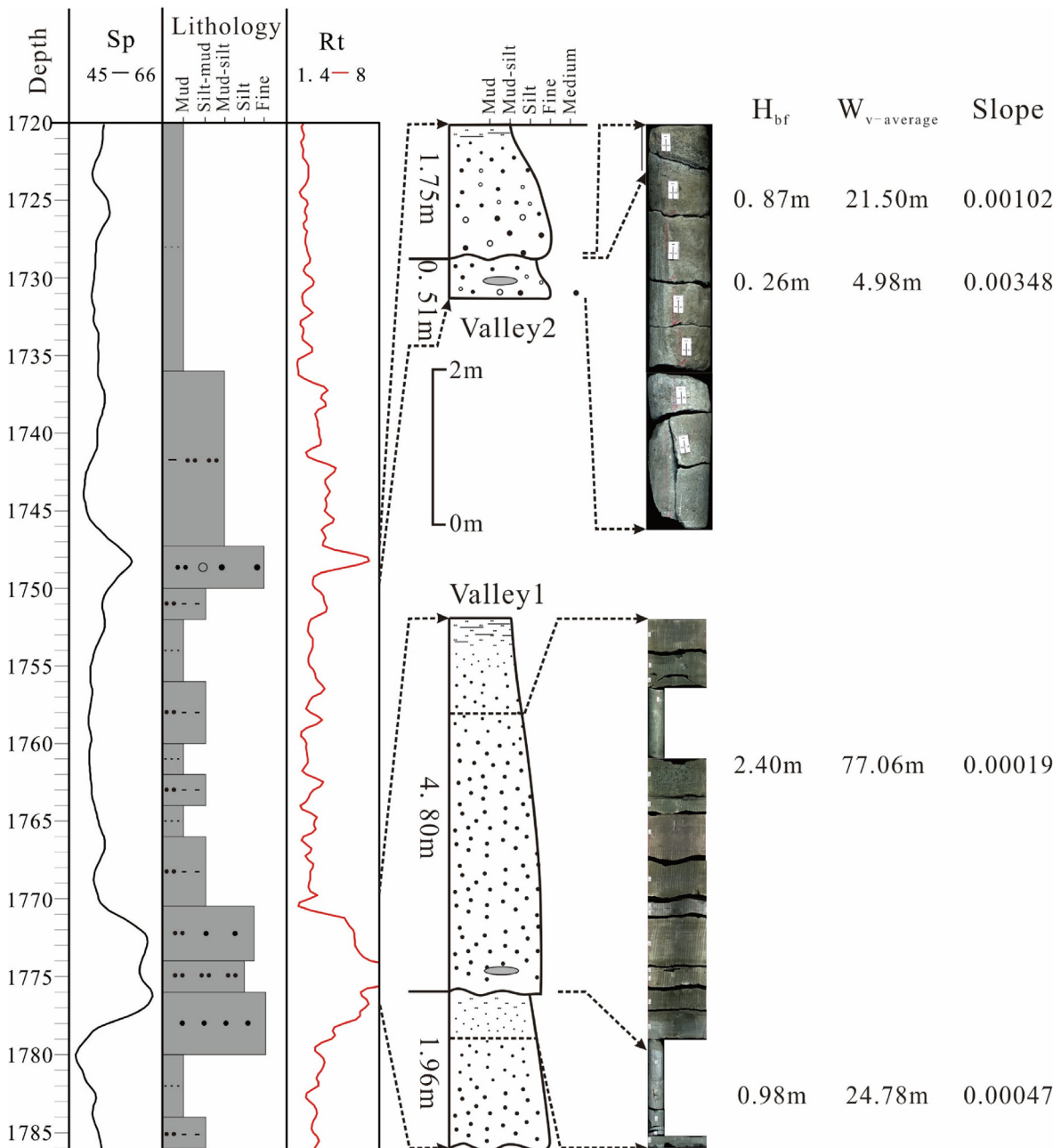


Fig. 7. The X016 valley section with thickness shown on the y-axis and geometric characteristics shown to the right. H_{bf} = average bankfull depth = 1/2 valley story thickness; $W_{v-average}$ = bankfull channel width.

northeast from Epoch 1 to Epoch 3 during the TST stage (Figs. 5A–C, 11A–C). According to the evolution of the source area, the uplift size continues to decrease during the TST stage from Epoch 1 to Epoch 3 (Fig. 12). In this way, the size that was not estimated at the beginning of the TST stage can be inferred to have been the largest (see Fig. 15).

After the evolution of the TST stage, the source area becomes small with few high relief and steep gradient area in the northeastern part of the source area at the beginning of the RST stage (Fig. 11D). Subsequently, the basement uplifts as a whole weakly as the region enter the tectonic activity quiescent period (Jiang et al., 2009; Yang, 2011; Yang and Miall, 2010). The basement uplifting combined with the drier climate makes the base level fall. The source area expands along with the base level fall. Due to the weak uplifting, the gradient of the expansion is stable (Fig. 5D–E, 11D–F). Therefore, the source area is much smaller during the RST than during the TST stage (Fig. 12).

5.3. Sediment discharge response

The sediment discharge is critical to understanding the down-system evolution (Allen et al., 2013; Bhattacharya et al., 2016). To quantify the sediment discharge response to the source area evolution, this research introduced a modified fulcrum approach (Holbrook and Wanas, 2014; Lin and Bhattacharya, 2017; Sharma et al., 2017). The bankfull valley dimensions of X016 were applied here to estimate the bankfull water discharge (Q_{bf}), bankfull bedload discharge (Q_{tbf}) and bankfull suspended discharge (Q_{ss}). As the bankfull discharge mainly controls the sediment supply, this research estimated only the bankfull discharge to reflect the sediment supply from the source area (Holbrook and Wanas, 2014; Lin and Bhattacharya, 2017; Sharma et al., 2017). The bankfull valley dimensions and the calculation results are summarized in Table 1 (Figs. 7 and 12). The sediment discharges during only Epoch 2 and Epoch 3 can be estimated because valley only fillings

Table 1
Paleohydrologic and discharge estimates from X016 valley fills.

Valley	Max/Min	Valley Story Thickness (m)	H _{bf} (m)	W _{v,average} (m)	W _v (Bridge and Mackey, 1993) (m)	W _v (Leopold and Maddock, 1953) (m)	S (10 ⁻³)	D16 (mm)	D50 (mm)	D84 (mm)	D90 (mm)	Water Discharge Q _{bf} (m ³ /s)	Bedload Discharge Q _{tblf} (m ³ /s)	Suspended Load Discharge Q _{ss} (m ³ /s)	Q _{total} (m ³ /s)
Valley 1	Max	4.80	2.40	77.06	43.23	110.89	0.19	0.02	0.15	0.45	0.58	170.9396	0.0095	0.1606	0.1701
	Min	1.96	0.98	24.78	8.48	41.07	0.47	0.15	0.29	0.63	0.80	22.3807	0.0019	0.0295	0.0314
Valley 2	Max	1.75	0.87	21.50	6.87	36.12	1.02	0.15	0.29	0.63	0.80	184.6375	0.0042	0.1242	0.1285
	Min	0.51	0.26	4.98	0.73	9.24	3.48	0.15	0.29	0.63	0.80	6.6413	0.0005	0.0120	0.0125

of Epoch 2 and Epoch 3 are preserved. The bankfull water discharge (Q_{bf}) ranged from 240.97 m³/s to 271.92 m³/s from Epoch 2 to Epoch 3. The change in the bankfull water discharge (Q_{bf}) suggests that the climate became wetter in the TST stage. The bankfull bedload discharge (Q_{tblf}) and bankfull suspended discharge (Q_{ss}) both decreased from Epoch 2 to Epoch 3, which indicates a decreasing tendency of the total bankfull sediment discharge (Fig. 12, Table 1).

The calculation method is an advantageous tool to reveal the sediment discharge of the source area. However, the sediment discharge calculation may involve several uncertainties, including measurements of valley geometry, numerical assessments used to estimate paleohydrologic parameters, and applicability of empirical equations (Lin and Bhattacharya, 2017). At the same time, only the sediment discharges of Epoch 2 and Epoch 3 can be estimated from core data. The integration of these imperfections constrains the accuracy of the sediment discharge estimation. However, the calculation can be used to state the tendency as error analysis of the method shows an error of small order (Bhattacharya et al., 2016; Lin and Bhattacharya, 2017). Therefore, this research attempted to reconstruct the semiquantitative evolution of the sediment discharge constrained by the bankfull sediment discharge calculation and other factors. The source area was selected as the first order factor since the source area size exerts a first-order control on the sediment discharge (Bhattacharya et al., 2016; Sømme et al., 2009). In addition, climate evolution which plays a role in controlling sediment discharge, was also considered (Bhattacharya et al., 2016; Densmore et al., 2007; Sømme et al., 2009). The largest source area produces a sufficient sediment discharge during Epoch 1, even though the climate is relatively dry during Epoch 1 of the TST stage (Figs. 2 and 12). During Epoch 2 and Epoch 3, the shrinking source area produces a decreasing sediment discharge (decreasing from 0.1701–0.0314 m³/s to 0.1285–0.0125 m³/s), even though the water discharge increases under the wetter climate (Figs. 2 and 12).

In the RST stage, the sediment discharges fluctuate across a range of low values in response to the small source area size, the increasingly drier climate and the low water discharge (Figs. 2 and 12). Although the increasingly drier climate hinders the production of sediment, the expanding source area increases the sediment discharges from Epoch 4 to Epoch 6 (Figs. 2 and 12).

Spatially, with high relief, steep gradient and exposed area mainly locate in the northeastern uplift, the sediment discharges mainly concentrate to the northeast of the source area. The distribution of the valleys well verifies the distribution of the sediment discharge. This topic is discussed in the next section.

5.4. Transfer system response

The valleys respond to the source area evolution and its sediment discharge. Surface dynamic processes (tectonic activity and climate) shape the valleys into different geometries with different fillings, as well as the source area (Blum et al., 2013). The valleys not only reflect the source area evolution and its sediment discharge but also indicate the system size and distribution (Bhattacharya et al., 2016; Sømme et al., 2009; Zhu et al., 2011). Therefore, both the valley geometry and filling are discussed to verify the evolution of the source area and sediment discharge and to constrain the reconstruction of the sink system.

5.4.1. Responses of valley distribution and geometry

The evolution and sediment discharge of a source area control the development of valleys (Bhattacharya et al., 2016; Sømme et al., 2009). Valleys develop well during the TST stage because the source area is high and large with powerful sediment discharge (Figs. 4A, 6A). In contrast, valleys don't develop under low sediment discharge produced by low and small source areas (Figs. 4B, 6A). Moreover, the sediment discharges that is concentrated in the northeastern source area lead to valley development in the same area (Fig. 4A). The above relation shows that the distribution of valleys responds to the topography of the

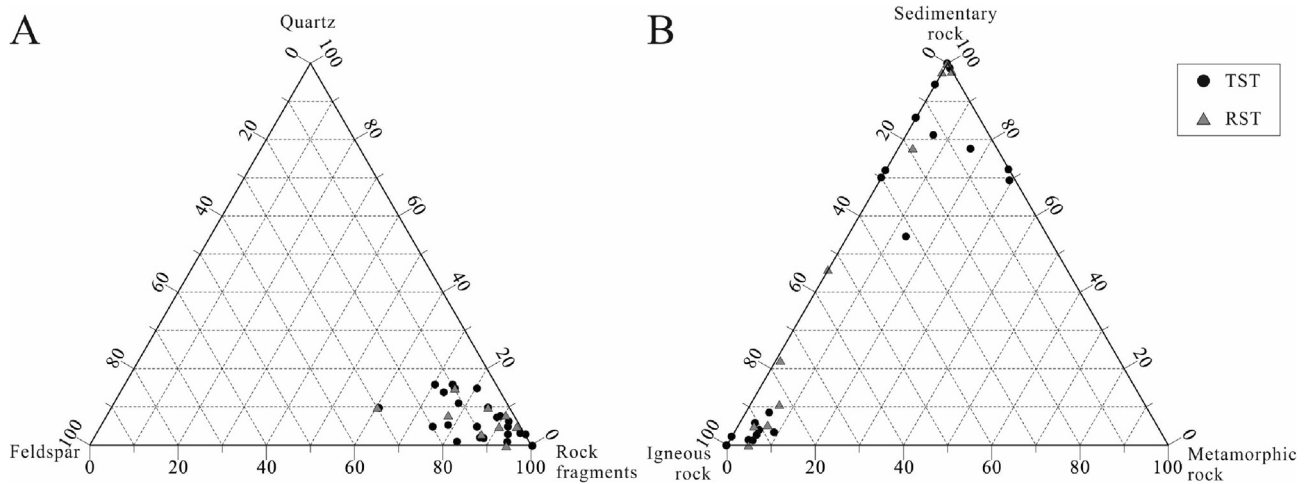


Fig. 8. (A) Composition of sediments and (B) types of rock fragments.

source area in time and space. In terms of the valley geometry, the bankfull depths and widths decrease from Epoch 2 to Epoch 3 with the decreasing sediment discharge in the shrinking source area (Figs. 6A, 7, Table 1). Moreover, the valley gradients mainly steepen in the northern part of the source area with steep gradient and high relief migrate to the north of the source area.

5.4.2. Response of valley fills

In the research area, most valleys developed without an Epoch 1 fill (Fig. 6A). During Epoch 1, the topography in the northern source area was gentler than the topography during Epoch 2 and Epoch 3. The difference in the topography leads to the production of finer sediments from the northern source area (Holbrook and Wanas, 2014). Although the hydrodynamic force is weak with a gentle topography and low water discharge, the fine sediments are easily carried directly to the sink without pauses (Fig. 6A). From Epoch 2 to Epoch 3, the steepening gradient of the northern source area produces coarsening sediments (Fig. 7, Table 1). Although the hydrodynamic force becomes strong with the steepening topography and increasing water discharge, coarser sediments are partly carried. With the coarsening of the sediments, more coarse sediments settle and result in the coarsening valley fillings (Fig. 7, Table 1). During the RST stage, the valleys have been filled and leveled.

5.5. Sedimentary effects and “source-to-sink” system evolution

5.5.1. Sedimentary paleogeomorphological evolution

The sedimentary paleogeomorphology affects the type and distribution of sand bodies (Dong et al., 2016). Therefore, the sedimentary paleogeomorphology is first discussed. Although only the integral sedimentary paleogeomorphology of the TST stage and the RST stage were shown, the source area evolution and tectonic evolution of the research area provided powerful tools for revealing the evolution of the sedimentary paleogeomorphology. Then, the evolution of the paleogeomorphology can be used to discuss the type and distribution of sand bodies.

During the TST stage, the slope gradients decreased from the bottom surface to the MFS (Fig. 3B). That indicates the paleogeomorphology becomes gentle with strong basement subsidence under the strong tectonic compression (Xian et al., 2017). Meanwhile, the continued strong subsidence leads to a lower topography. However, the above process becomes weak as the strength of the tectonic activity decreases during the TST stage. The spatial patterns of paleogeomorphology also change with the source area evolution, which is controlled by the difference in the strength of the faulting of TST stage. With the strong faulting of the North Beisantai Fault, the steeper slopes mainly locate in

the northern area and the lower topographies mainly locate in the footwall of the North Beisantai Fault in the north-south direction. The above process responds to the high relief and steep gradient migration of the source area to the north and makes the northern area steeper and lower than the southern area at the same distance from the uplift (Figs. 3B, 4A, 11A–C). In the east-west direction, the strong faulting in the east direction produces steeper slopes mainly located in the eastern area and lowers the topographies in the footwall of the eastern North Beisantai Fault and Xiquan Fault. This evolution, combined with the smoothing processes of paleogeomorphology, causes the steep slopes and the low topographies to narrow in the northeastern area near the source area from Epoch 1 to Epoch 3 (Figs. 4, 11A–C). Moreover, as the southwestern source area atrophies, gentle slopes develop with an expanding tendency in the southwestern area. The gentle slopes in the southwestern area are higher than those in other areas due to the high relief of the early stage. The above processes all imply that steep slopes and low topographies develop only in the northeastern area near the source area in the RST stage (Fig. 4B). Obviously, the gentle slopes expand during the TST stage. However, the gentle slopes with relatively high relief narrow with the lowering of the topographies. Note that most slopes are relatively steep and high until the end of the TST stage, even though the topographies are becoming gentle and low.

By the RST stage, the smoothing and lowering processes of the TST stage limit the steep slopes and low paleogeomorphology to a small area in the northeastern region near the source area (Fig. 4B). Gentle slopes with relatively low relief develop widely in the southwestern area (Fig. 4B). Then, the basement rebounds and lifts the paleogeomorphology as a whole. The slope gradients basically remain stable from the MFS surface to the top surface during the RST stage (Fig. 3B). In contrast, the high relief expands under the basement rebounding. As the topographies are higher in the southern and western areas, the high relief expands mainly to the south and west. In this process, the high slopes with gentle gradients mainly expand to the south and west (Fig. 4B). In the northern area, few high slopes with gentle gradients developed because the topographies are lower than that in other areas (Fig. 4B).

5.5.2. Effects on sand body type

Significant differences in the major sand body type developed between the TST stage and the RST stage. Based on the above discussion, the genesis of different effects on the sand body type were revealed. The steeper sedimentary paleogeomorphology promotes the development of fan deltas during the TST stage (Figs. 4A, 14A–C). However, the steep slopes limit the development of beach bars (Fig. 4A, 14A–C) (Jiang et al., 2011). On the other hand, the gentle slopes of the TST stage are also not suitable for beach bar development because the

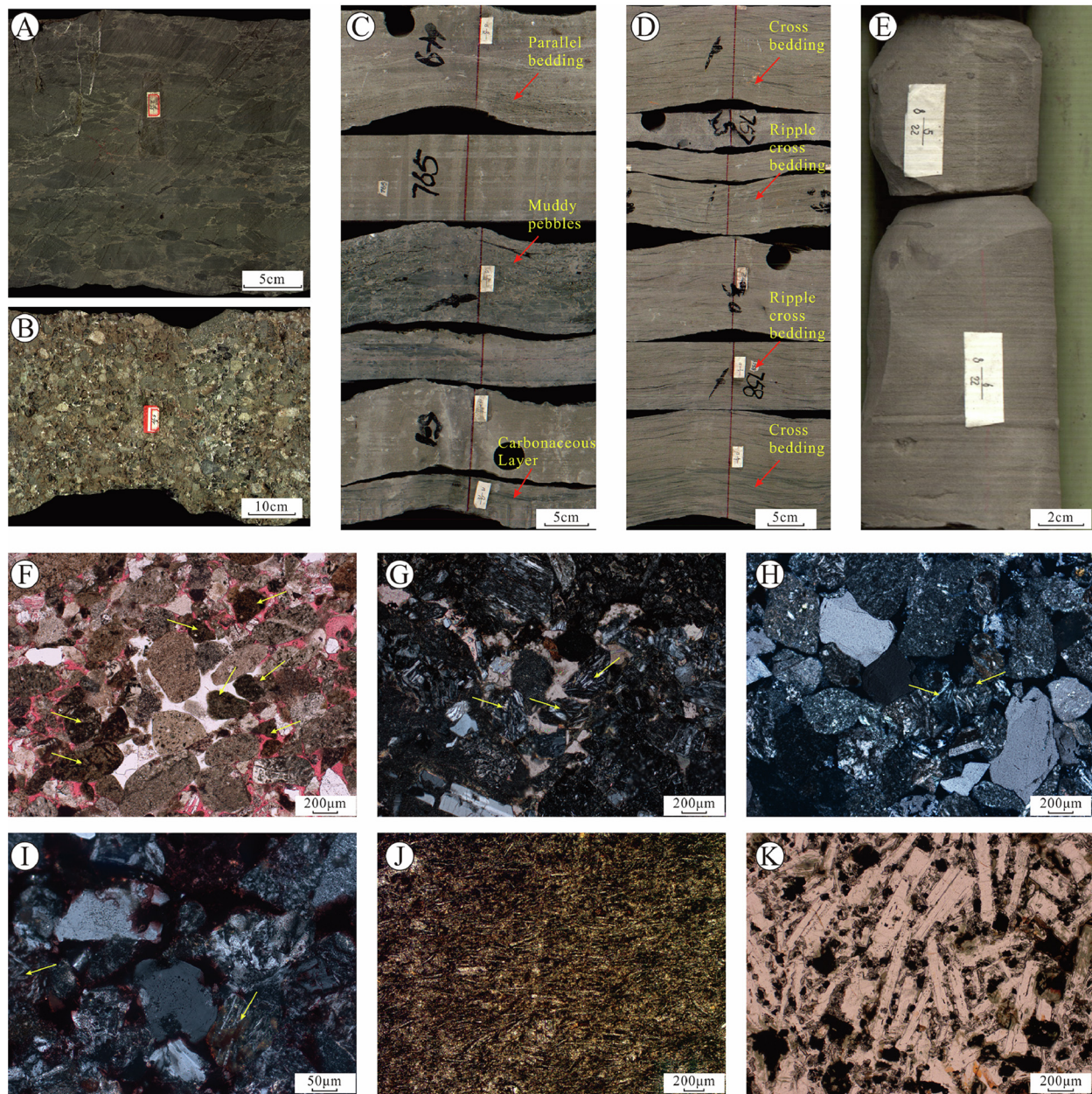


Fig. 9. (A) Pebble sandstone that mainly consists of muddy pebbles with poor sorting and roundness; B69, 1590.66 m, TST stage. (B) Pebble sandstone that consists of muddy and igneous pebbles with relatively poor sorting and roundness; B69, 1674.85, TST stage. (C) Pebble fine-medium sandstone with poor sorting and roundness comprising muddy pebbles and fine sandstone with parallel bedding and carbonaceous layers; B42, 2048 m, TST stage. (D) Silt to fine-grained sandstone with cross-bedding and ripple cross-bedding; B42, 2042.56 m, RST stage. (E) Mudstone of the Middle Permian Pingdiquan Formation preserved on the uplift; B15, 2650.92 m. (F) Muddy rock fragments shown in plane-polarized light; B42, 2107.12 m, TST stage. (G) Mafic extrusive rock fragments shown in cross-polarized light; B37, 2677.5 m, TST stage. (H) Intermediate extrusive rock fragments shown in cross-polarized light; B89, 2242.69 m, TST stage. (I) Mafic and intermediate extrusive rock fragments shown in cross-polarized light; B20, 2102.53 m RST stage. (J) Andesitic texture of Carboniferous andesite shown in plane-polarized light; X5, 2922.28 m. (K) Intergranular texture of Carboniferous basalt shown in plane-polarized light; B5, 2633 m.

lowering process and wet climate cause deep-water conditions above the gentle slopes (Fig. 4A). Therefore, few beach bars develop in the limited available space (Fig. 14A–C). During the RST stage, the different sedimentary paleogeomorphology changes the dominant sand body type. Beach bars develop well as more gentle slopes with slightly high relief develop under shallow-water conditions (Fig. 4B, 14D–F). In contrast, fan deltas are limited by the gentle paleogeomorphology (Fig. 4B, 14D–F). Obviously, the sedimentary paleogeomorphology controls the type of sand body.

5.5.3. Spatial and temporal distributions of sand bodies and “source-to-sink” system evolution

The segments of the upstream system controls the spatial and temporal distributions of sand bodies (Allen et al., 2013; Armitage et al., 2011; Densmore et al., 2007; Dong et al., 2016; Whittaker et al., 2011). Based on the system reconstruction of upstream areas and sedimentary paleogeomorphology, the spatial and temporal distributions of sand bodies can be well demonstrated through the six stratal slices and their root mean square (RMS) attributes (Figs. 13 and 14). The preserved sediment volumes of sand bodies were also applied to reveal the spatial and temporal distributions of sand bodies and variations in

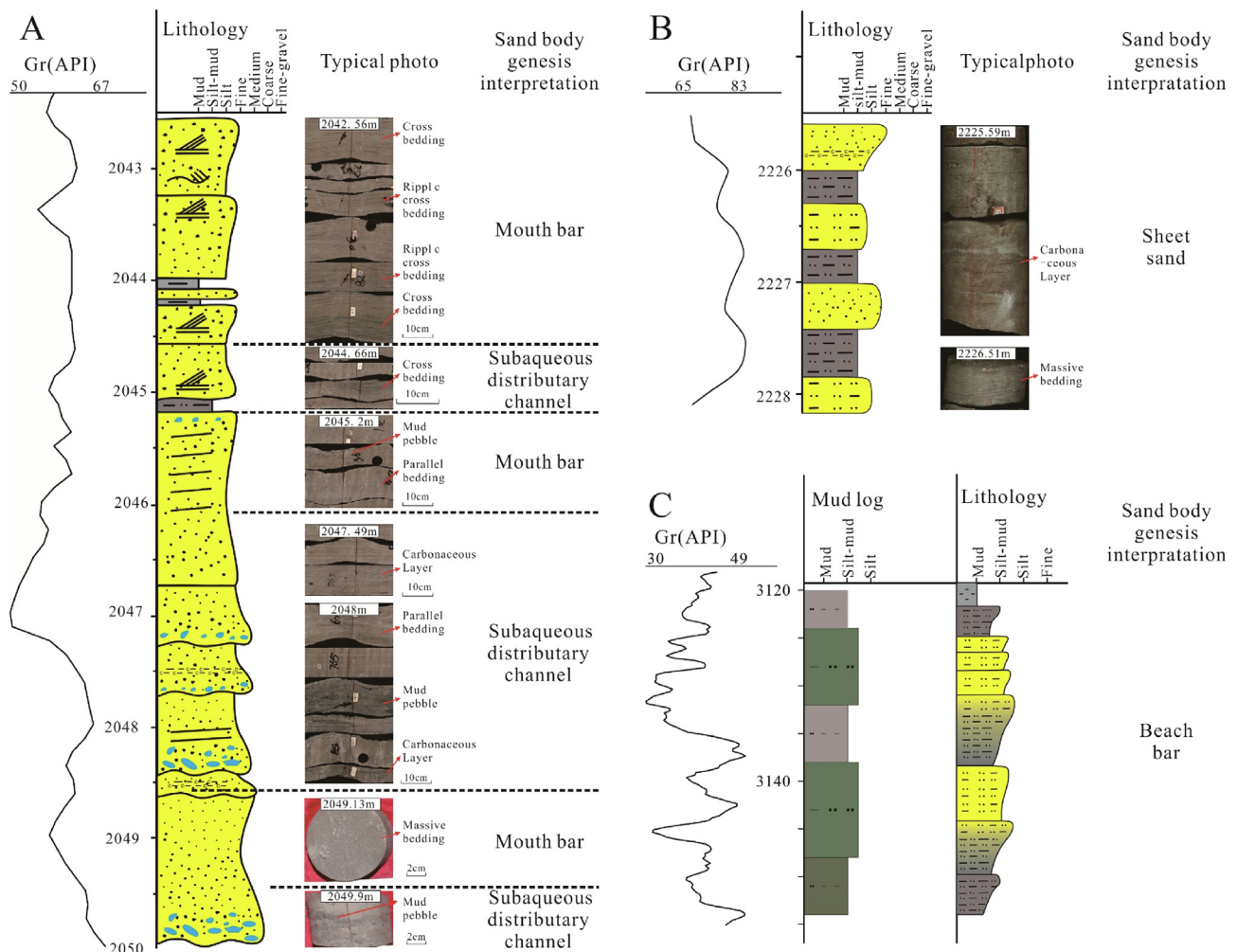


Fig. 10. The sedimentary characteristics of each sand body type: (A) subaqueous distributary channel and mouth bar in the B42 log, (B) sheet sands in the B52 log, and (C) beach bars in the B47 log.

the sediment discharge (Fig. 12, Table 1) (Sømme et al., 2011). Moreover, the “source-to-sink” system evolution is reconstructed.

During Epoch 1 of the TST stage, the largest source area produces a sufficient sediment discharge, even though the climate is relatively drier (Figs. 2 and 12). The powerful sediment discharges form the largest and gentlest valleys of the TST stage. The sediment discharges mainly consist of fine sediments due to the gentle slopes of valleys. This powerful and fine sediment discharges are transported directly into the sink without being deposited in the valleys. This process finally constructs the largest scale sand bodies with a volume of $13.24 \times 10^9 \text{ m}^3$ (Figs. 12 and 14A, Table 2). As steep slopes develop widely, fan deltas dominate the sand body types with a volume of $11.84 \times 10^9 \text{ m}^3$ (Figs. 12 and 14A, Table 2). With spatial differences in faulting, the high relief and steep gradient that develop in and near the northeastern source area concentrate the sediment discharges and valleys in the northeastern area (Fig. 11A). As the steep gradient have not yet migrated to the northern source area, slightly coarse sediments develop and are transported through the valleys without being deposited (Figs. 6A, 7). Most sediments are transported to northeastern region to construct fan deltas in the steep paleogeomorphology setting (Figs. 14A, 15A). In other areas, the slightly high relief and steep gradient produce small exposed areas with few valleys. The sediment discharges is weak. With slightly steep slopes, fan deltas develop on a small scale in the other areas (Figs. 4A, 14A, 15A). In addition, few sediments are transported to parts of the southern areas, where gentle and low slopes develop, and small-scale beach bars are deposited

(Figs. 4A, 14A, 15A).

During Epoch 2 of the TST stage, the basement subsidence and the wetter climate lift the base level and narrows the source area (Figs. 2, 5A, 12). The sediment discharges decrease, even though the climate becomes wetter (Figs. 2, 12, Table 1). The steep gradient and high relief narrow to the northeastern part of the source area under faulting of different strengths. Coarser sediments are produced in the northern source area where the gradient was steeper (Fig. 7). When sediments are transported through the valleys, the coarser sediments fill and narrow the valleys during this epoch (Figs. 6A, 7). Then, the rest of the sediments enter the sink and construct reduced sand bodies with a volume of $11.65 \times 10^9 \text{ m}^3$ (Figs. 12, 14B, Table 2). Fan deltas are still the major sand body with a volume of $10.88 \times 10^9 \text{ m}^3$ (Figs. 12, 14B, Table 2). The narrowed steep slopes and decreasing sediment discharge limit the development of fan deltas. In contrast, the expansion of gentle slopes provides more available space for the development of beach bars. However, the deeper-water conditions resulting from the lower topographies and wet climate cause the beach bars to shrink to a volume of $0.77 \times 10^9 \text{ m}^3$ (Figs. 12, 14B, Table 2). Spatially, because the sediment discharges and paleogeomorphology inherit the spatial attributes of Epoch 1, the sediment discharges from the valleys concentrate the fan deltas mainly to the north of the source area (Figs. 14B, 15B). Few fan deltas develop to the south of the source area. The beach bars migrate to the south and west along with the slopes become gentle in the southwestern area (Figs. 14B, 15B).

In Epoch 3 of the TST stage, although the climate is the wettest, the

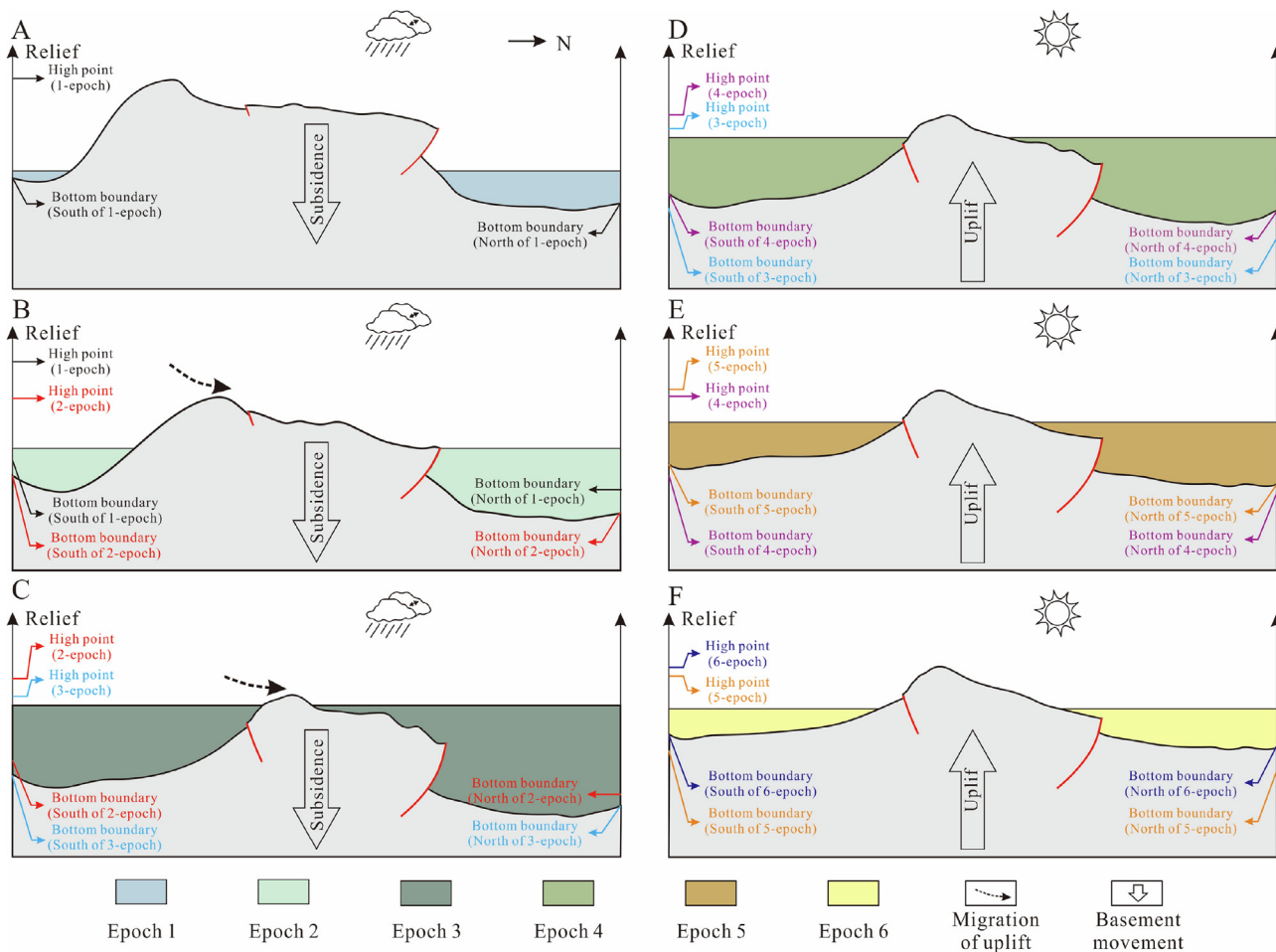


Fig. 11. Evolution of the source area for the period from Epoch 1 to Epoch 6 (A-F).

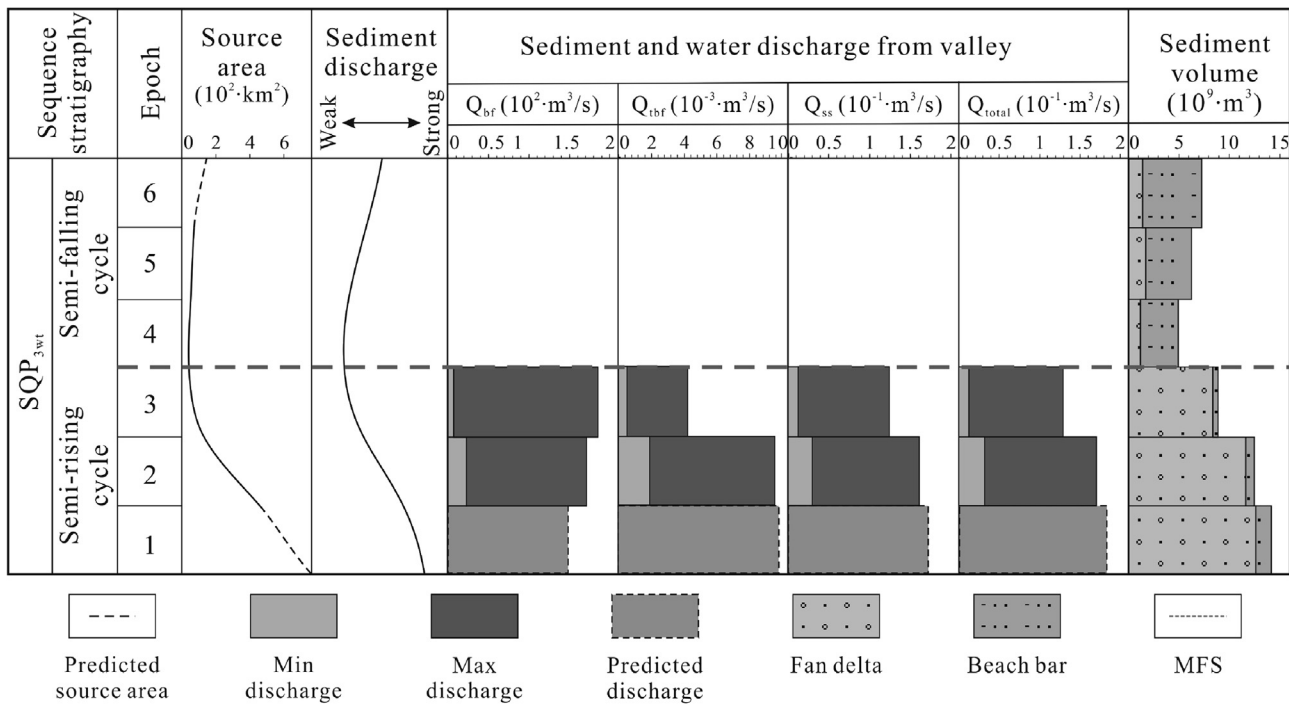


Fig. 12. Sediment discharge and volume characteristics for the late Permian. Q_{bf} = bankfull water discharge; Q_{tbf} = bankfull bedload discharge; Q_{ss} = bankfull suspended load discharge. Q_{total} is the sum of Q_{tbf} and Q_{ss}.

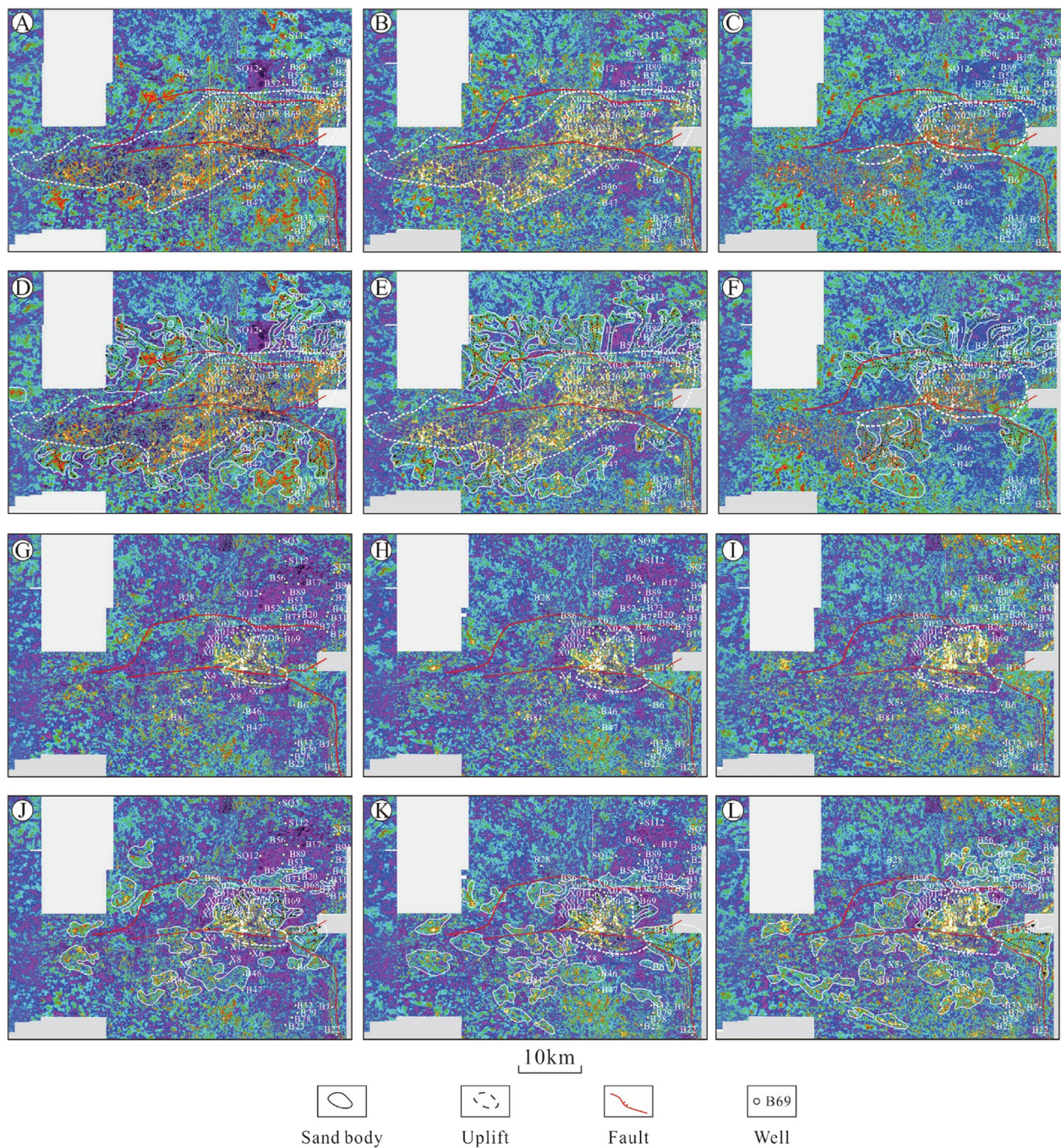


Fig. 13. The root mean square (RMS) amplitude map and interpreted sand body boundary of every stratal slice SQP_{3wr} . (A–C), RMS map of Epochs 1–3; (D–F), the sand body boundary of Epochs 1–3; (G–I), the RMS map of Epochs 4–6; (J–L), the sand body boundary of Epochs 4–6. The source area cannot be estimated at the beginning of Epoch 1 and end of Epoch 6, so the source area size at the end of Epoch 1. The map shows only the system sourced from the Beisantai Uplift.

small source area limit the sediment discharges to low levels (Figs. 2, 5B, 12, Table 1). The grain sizes of the sediments evolve in the same manner as those in Epoch 1 and Epoch 2. With continued steepening of the northern source area, the valleys are further filled and narrowed by more coarsened sediments (Figs. 6A, 7). Then, the limited sediment discharges construct the smallest sand bodies of the TST stage, with a volume of $8.32 \times 10^9 \text{ m}^3$ (Figs. 12, 14C, 15C). Meanwhile, with the later evolution following the same tendency as that in Epoch 2, fan deltas are further limited, with a volume of $7.83 \times 10^9 \text{ m}^3$ mainly concentrates to the north of the source area (Figs. 12, 14C, 15C). Moreover, the beach bars shrink in a volume of $0.49 \times 10^9 \text{ m}^3$ as the water conditions become deep and migrate to the south and west with the slopes become gentle in the southwestern area (Figs. 12, 14C, 15C).

At the beginning of the RST stage, the source area is reduced to its smallest scale with the base level rise of the TST stage (Figs. 2, 5C, 12). With the basement uplift and dry climate from Epoch 4 to Epoch 6, the base level falls and expands the source area weakly (Fig. 12). The expanded source area produces slightly increasing sediment discharge (Fig. 12). This change results in the somewhat expanded scale of the sand bodies (Fig. 14D–F). The volume increased from $4.60 \times 10^9 \text{ m}^3$ to $6.79 \times 10^9 \text{ m}^3$ (Fig. 12, Table 2). Combining with the expansion of gentle slopes and the weakly high relief to the south and west, beach bars expand and migrate to the south and west, with the volume increasing from $3.55 \times 10^9 \text{ m}^3$ to $5.53 \times 10^9 \text{ m}^3$ (Figs. 4B, 12, 14D–F, 15D–F, Table 2). Meanwhile, the development of fan deltas is limited by the expansion of gentle slopes (Figs. 4B, 12, 14D–F). The fan deltas

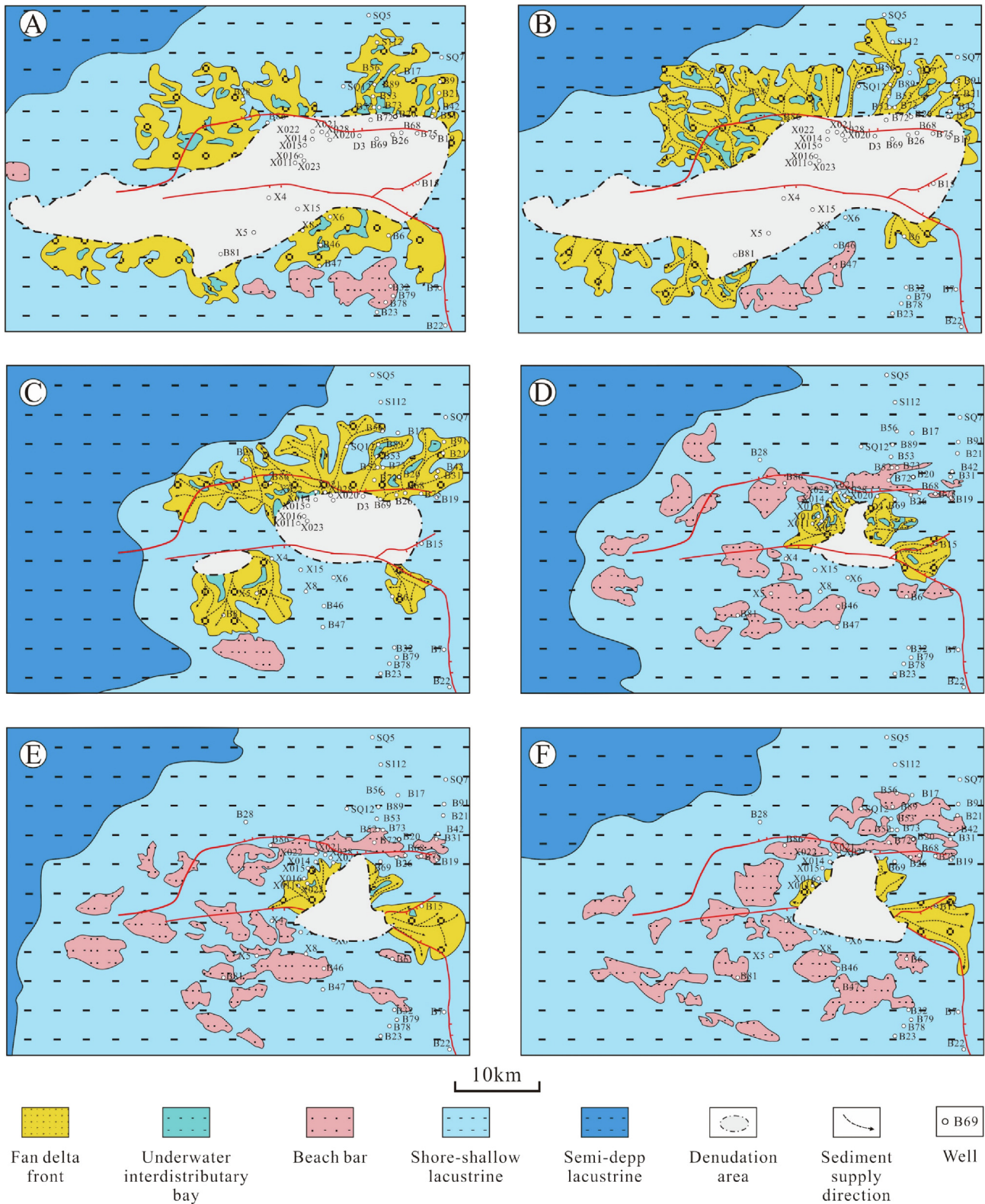


Fig. 14. Sediment dispersal patterns of every stratal slice from Epoch 1 to Epoch 6 (A–F) as described in Fig. 13.

fluctuated in their distribution and volume near the source area (Fig. 14D–F, 15D–F). The volume ranged between $1.05 \times 10^9 \text{ m}^3$ and $1.57 \times 10^9 \text{ m}^3$ (Fig. 12, Table 2).

5.6. Factors of the “source-to-sink” system

The “source-to-sink” evolution reveals several factors that affect the systems and control different aspects of the sedimentary effects. The evolution trends of the sediment discharges are consistent with the evolution trends of the sediment volumes. The magnitude of the

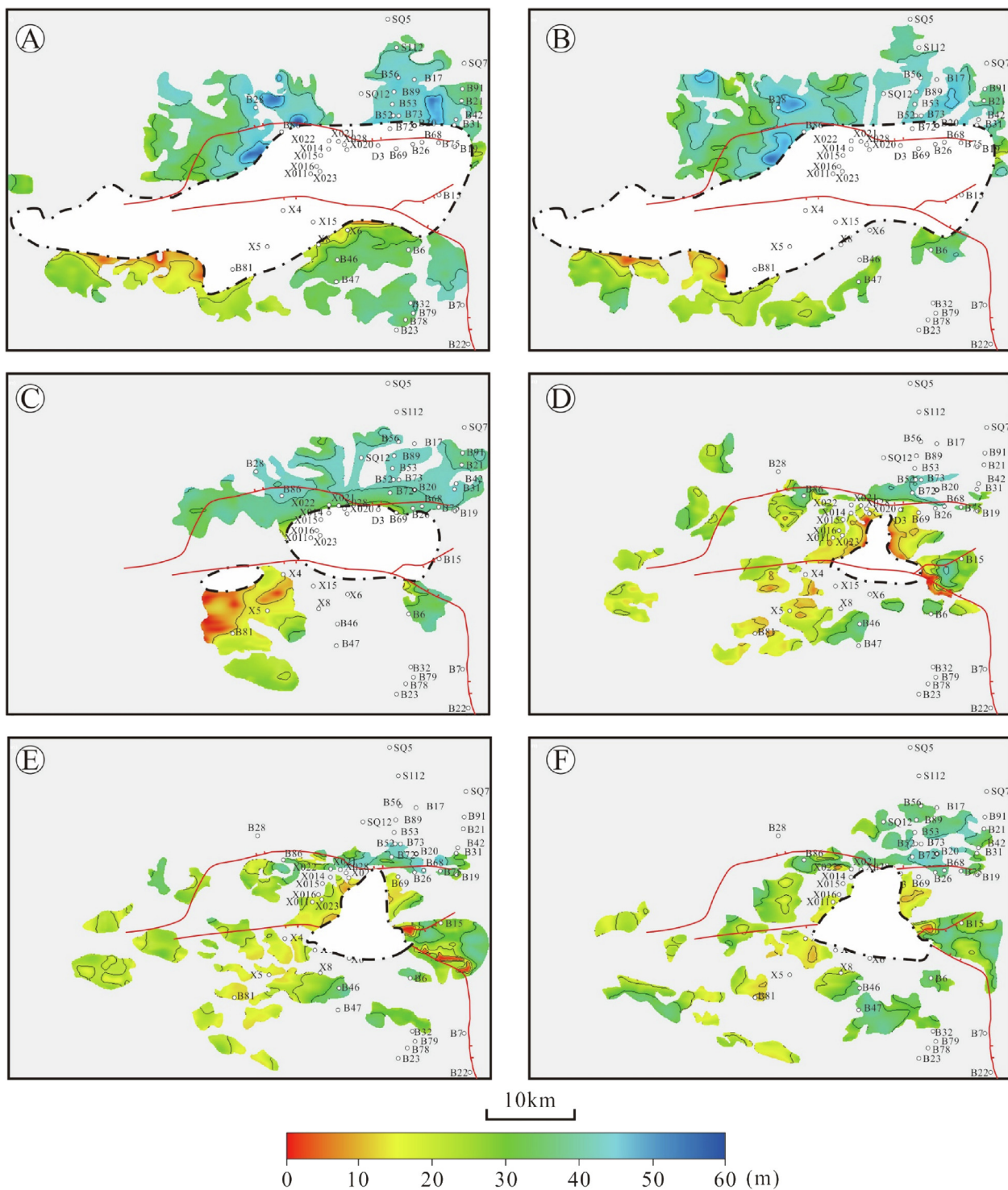


Fig. 15. Isochore thickness maps of sedimentary bodies used as the basis for volume calculations from Epoch 1 to Epoch 6 (A–F).

sediment discharges, which are mainly controlled by the source area size, determined the scale of the sand bodies. The sediment discharges finally construct the special temporal distribution of sand bodies concentrated in the TST stage. The spatial distribution of the sediment discharge, transfer system and sedimentary paleogeomorphology controls the spatial distribution of the sand bodies. Due to the sediment discharge, valleys are mainly located in the north of the source area. These valleys transport the powerful sediment discharges and constructed fan deltas under the steep paleogeomorphology setting in the same area. In contrast, the gentle slopes to the south and west of the

source area mainly promote the development of beach bars. Moreover, the sedimentary paleogeomorphology patterns determined the main sand body type. With the steeper sedimentary paleogeomorphology during the TST stage, fan deltas dominate the sand body types. In contrast, the RST stage mainly develop beach bars because the sedimentary paleogeomorphology was gentler. In general, all factors are linked with the source area. The evolution of the source area controlled these factors and finally determined the evolution of the system.

Table 2
Estimated sediment volume of the late Permian.

Epoch	Sediment Volume (10 ⁹ m ³)		
	Fan Delta	Beach Bar	Total
Epoch 1	11.84	1.40	13.24
Epoch 2	10.88	0.77	11.65
Epoch 3	7.83	0.49	8.32
Epoch 4	1.05	3.55	4.60
Epoch 5	1.57	4.26	5.83
Epoch 6	1.26	5.53	6.79

6. Conclusions

A comprehensive analysis of external perturbations and internal “source-to-sink” system responses was applied to reconstruct the characteristics and evolution of a “source-to-sink” system in this research. A number of new insights have been gained about the “source-to-sink” system in the Beisantai area.

First, the Beisantai Uplift supplies the system during the late Permian. During this period, sedimentary rock fragments and pebbles come from the Carboniferous and the Pingdiquan Formation of middle Permian.

Second, the Beisantai Uplift is not the thrust front uplift and cannot be completely described by the flexural deformation of either an elastic lithosphere or a viscoelastic lithosphere. During the TST stage, the uplift atrophies. Most southern and western part of uplift are submerged. During the RST stage, the source area expanded.

Third, the source area evolution under tectonic and climatic perturbations controls the magnitude and spatial distribution of the sediment discharge. The source area size exerts a first-order control on the magnitude of the sediment discharge. The paleogeomorphology of the source area controls the spatial distribution of the sediment discharge.

Fourth, the distribution, geometry and filling of valleys responds to the source area evolution. The high reliefs, steep gradients and strong sediment discharges in the northern part of the source area cause valleys to be concentrated to the north during the TST stage. Moreover, the steepening of the northern source area causes coarsened sediments to fill the valleys.

Finally, the source area determines the system evolution by controlling the sediment discharge, transfer system and sedimentary paleogeomorphology. The magnitude of sediment discharges determines the scale of the sand bodies. The spatial distribution of the sediment discharge, transfer system and sedimentary paleogeomorphology determines the spatial distribution of the sand bodies. Moreover, the sedimentary paleogeomorphology determines the main sand body types.

Declaration of Competing Interest

None

Acknowledgments

This work was co-funded by the National Nature Science Foundation of China (grant no. U1762217, grant no. 41402095), the Fundamental Research Funds for the Central Universities (18CX05027A), the National Science and Technology Special Projects of China (2017ZX05009001), the Strategic Priority Research Program of the Chinese Academy of Sciences (grant no. XDA14010301), and the Scientific and Technological Innovation Project financially supported by the Qingdao National Laboratory for Marine Science and Technology (no. 2015ASKJ01). Thanks to the Xinjiang Oilfield, PetroChina, for providing background geologic data.

Appendix A. Supplementary material

Supplementary data to this article can be found online at <https://doi.org/10.1016/j.jseas.2019.103907>.

References

- Allen, P.A., Armitage, J.J., Carter, A., Duller, R.A., Michael, N.A., Sinclair, H.D., Whitchurch, A.L., Whittaker, A.C., 2013. The Qs problem: Sediment volumetric balance of proximal foreland basin systems. *Sedimentology* 60, 102–130. <https://doi.org/10.1111/sed.12015>.
- Armitage, J.J., Duller, R.A., Whittaker, A.C., Allen, P.A., 2011. Transformation of tectonic and climatic signals from source to sedimentary archive. *Nat. Geosci.* 4, 231–235. <https://doi.org/10.1038/ngeo1087>.
- Beaumont, C., Quinlan, G., Hamilton, J., 1988. Orogeny and stratigraphy: numerical models of the Paleozoic in the eastern interior of North America. *Tectonics* 7, 389–416. <https://doi.org/10.1029/TC007i003p00389>.
- Bhattacharya, J.P., Copeland, P., Lawton, T.F., Holbrook, J., 2016. Estimation of source area, river paleo-discharge, paleoslope, and sediment budgets of linked deep-time depositional systems and implications for hydrocarbon potential. *Earth-Sci. Rev.* 153, 77–110. <https://doi.org/10.1016/j.earscirev.2015.10.013>.
- Blum, M., Martin, J., Milliken, K., Garvin, M., 2013. Paleovalley systems: insights from Quaternary analogs and experiments. *Earth-Sci. Rev.* 116, 128–169. <https://doi.org/10.1016/j.earscirev.2012.09.003>.
- Bridge, J.S., Tye, R.S., 2000. Interpreting the dimensions of ancient fluvial channel bars, channels, and channel belts from wireline-logs and cores. *Am. Assoc. Pet. Geol. Bull.* 84, 1205–1228. <https://doi.org/10.1306/E4FD4B07-1732-11D7-8645000102C1865D>.
- Cai, Z., Chen, F., Jia, Z., 2000. Types and tectonic evolution of Junggar basin. *Earth Sci. Front.* 7, 431–440.
- Carvajal, C., Steel, R., 2012. Source-to-sink sediment volumes within a tectono-stratigraphic model for a laramide shelf-to-deep-water basin: methods and results. *Tectonics Sediment. Basins Recent Adv.* 131–151. <https://doi.org/10.1002/9781444347166.ch7>.
- Chen, S., Zhang, Y., Tang, L., 2001. Evolution of Junggar Late Carboniferous-Permian foreland basin. *J. Univ. Pet. China* 25, 11–15.
- Crampton, S.L., Allen, P.A., 1995. Recognition of forebulge unconformities associated with early stage foreland basin development: example from the north Alpine foreland basin. *Am. Assoc. Pet. Geol. Bull.* 79, 1495–1514.
- Deng, H., Xiao, Y., Ma, L., Jiang, Z., 2011. Genetic type, distribution patterns and controlling factors of beach and bars in the second member of the Shahejie formation in the Dawangbei Sag, Bohai Bay. *China. Geol. J.* 46, 380–389. <https://doi.org/10.1002/gj.1290>.
- Densmore, A.L., Allen, P.A., Simpson, G., 2007. Development and response of a coupled catchment fan system under changing tectonic and climatic forcing. *J. Geophys. Res.* Earth Surf. 112, 1–16. <https://doi.org/10.1029/2006JF000474>.
- Dong, G., He, Y., Leng, C., Gao, L., 2016. Mechanism of sand body prediction in a continental rift basin by coupling paleogeomorphic elements under the control of base level. *Pet. Explor. Dev.* 43, 579–590. [https://doi.org/10.1016/S1876-3804\(16\)30068-4](https://doi.org/10.1016/S1876-3804(16)30068-4).
- Fang, S.H., Jia, C.Z., Guo, Z.J., Song, Y., Xu, H.M., Lou, J.L., 2006. New view on the Permian evolution of the Junggar basin and its implications for tectonic evolution. *Earth Sci. Front.* 12, 108–121.
- Feng, Y., Jiang, S., Wang, C., 2015. Sequence stratigraphy, sedimentary systems and petroleum plays in a low-accommodation basin: Middle to upper members of the Lower Jurassic Sangonghe Formation, Central Junggar Basin, Northwestern China. *J. Asian Earth Sci.* 105, 85–103. <https://doi.org/10.1016/j.jseas.2015.03.025>.
- Flemings, P.B., Jordan, T.E., 1990. Stratigraphic modeling of foreland basins: interpreting thrust deformation and lithosphere rheology. *Geology* 18, 430–434. [https://doi.org/10.1130/0091-7613\(1990\)018<0430:SMOFBI>2.3.CO;2](https://doi.org/10.1130/0091-7613(1990)018<0430:SMOFBI>2.3.CO;2).
- Garzanti, E., 2017. The maturity myth in sedimentology and provenance analysis. *J. Sediment. Res.* 87, 353–365. <https://doi.org/10.2110/jsr.2017.17>.
- Helland-hansen, W., Sømme, T.O.R.O., Martinsen, O.L.E.J., Lunt, I.A.N., Thurmond, J., 2016. Deciphering Earth's natural hourglasses: perspectives on source-to-sink. *Anal. J. Sediment. Res.* 1008–1033.
- Holbrook, J., Wanas, H., 2014. A Fulcrum Approach to assessing source-to-sink mass balance using channel paleohydrologic parameters derivable from common fluvial data sets with an example from the cretaceous of Egypt. *J. Sediment. Res.* 84, 349–372. <https://doi.org/10.2110/jsr.2014.29>.
- Jia, H., Ji, H., Li, X., Zhou, H., Wang, L., Gao, Y., 2016. A retreating fan-delta system in the Northwestern Junggar Basin, Northwestern China-Characteristics, Evolution and controlling factors. *J. Asian Earth Sci.* 123, 162–177. <https://doi.org/10.1016/j.jseas.2016.04.004>.
- Jiang, H., Wang, H., Lu, Y., Zhao, Z., Chen, S., 2009. Dual features of sequence structures in compressional basin - an example from jurassic bohu depression of yanqi basin. *Acta Geol. Sin.* 83, 847–854.
- Jiang, Zaixing, Liu, H., Zhang, S., Su, X., Jiang, Zhonglong, 2011. Sedimentary characteristics of large-scale lacustrine beach-bars and their formation in the eocene boxing sag of bohai bay basin, east china. *Sedimentology* 58, 1087–1112. <https://doi.org/10.1111/j.1365-3091.2010.01196.x>.
- Jin, M., Tan, X., Tong, M., Zeng, W., Liu, H., Zhong, B., Liu, Q., Lian, C., Zhou, X., Xu, H., Luo, B., 2017. Karst paleogeomorphology of the fourth Member of Sinian Dengying Formation in Gaoshiti-Moxi area, Sichuan Basin, SW China: restoration and geological significance. *Pet. Explor. Dev.* 44, 58–68. <https://doi.org/10.1016/S1876->

- 3804(17)30008-3.
- Johnsson, M.J., 1993. The system controlling the composition of clastic sediments 1–20. <https://doi.org/10.1130/SPE284-p1>.
- Leopold, L.B., Maddock, T.J., 1953. The hydraulic geometry of stream channels and some physiographic implications. *Geol. Surv. Prof. Pap.* 252, 57. <https://doi.org/10.3133/PP252>.
- Li, D., Yang, J., Zhu, X., 2005. Study on the sequence stratigraphy of Zhungeer Basin. *J. Xi'an Shiyou Univ. (Natural Sci. Ed.)* 20, 60–66.
- Li, Y., Wei, D., Chen, Z., Jia, D., Ma, D., Wang, Y., Cui, J., Shen, S., 2016. Multiphase deformation deduced from 3D construction and restoration: Implication for the hydrocarbon exploration in the mountain front of the Northern Tianshan. *Mar. Pet. Geol.* 77, 916–930. <https://doi.org/10.1016/j.marpetgeo.2016.07.028>.
- Lin, W., Bhattacharya, J.P., 2017. Estimation of Source-To-Sink Mass Balance By A Fulcrum Approach Using Channel Paleohydrologic Parameters of the Cretaceous Dunvegan Formation. *Canada. J. Sediment. Res.* 87, 97–116. <https://doi.org/10.2110/jsr.2017.1>.
- Liu, H., Liang, H., Cai, L., Xia, Y., Liu, L., 1994. Evolution and structural style of Tianshan and adjacent basins. *Northwestern China. Earth Sci.* 19, 727–741.
- Margins Program, Science Plans 2004, 2003. New York.
- Plint, A.G., Wadsworth, J.A., 2003. Sedimentology and palaeogeomorphology of four large valley systems incising delta plains, western Canada Foreland Basin: implications for mid-Cretaceous sea-level changes. *Sedimentology* 50, 1147–1186. <https://doi.org/10.1111/j.1365-3091.2003.00599.x>.
- Reijnenstein, H.M., Posamentier, H.W., Bhattacharya, J.P., 2011. Seismic geomorphology and high-resolution seismic stratigraphy of inner-shelf fluvial, estuarine, deltaic, and marine sequences, Gulf of Thailand. *Am. Assoc. Pet. Geol. Bull.* 95, 1959–1990. <https://doi.org/10.1306/03151110134>.
- Ren, Y., Dele, Q., Tan, Q., Xu, X.L., Li, L., 2016. Provenance analysis of the Permian Wutonggu Formation in North 83 Well Block at Beisantai, Junggar Basin. *Acta Geol. Sichuan* 36, 54–59.
- Romans, B.W., Castellort, S., Covault, J.A., Fildani, A., Walsh, J.P., 2016. Environmental signal propagation in sedimentary systems across timescales. *Earth-Sci. Rev.* 153, 7–29. <https://doi.org/10.1016/j.earscirev.2015.07.012>.
- Schattner, U., Lazar, M., 2016. Hierarchy of source-to-sink systems—Example from the Nile distribution across the eastern Mediterranean. *Sediment. Geol.* 343, 119–131. <https://doi.org/10.1016/j.sedgeo.2016.08.006>.
- Sharma, S., Bhattacharya, J.P., Richards, B., 2017. Source-to-sink sediment budget analysis of the Cretaceous Ferron Sandstone, Utah, U.S.A., using the Fulcrum approach. *J. Sediment. Res.* 87, 594–608. <https://doi.org/10.2110/jsr.2017.23>.
- Shu, L.S., Zhu, W., Wang, B., Faure, M., Charvet, J., Cluzel, D., 2005. The post-collision intracontinental rifting and olistostrome on the southern slope of Bogda Mountains, Xinjiang. *Acta Petrol. Sin.* 21, 27–38.
- Sømme, T.O., Helland-hansen, W., Martinsen, O.J., Thurmond, J.B., 2009. Relationships between morphological and sedimentological parameters in source-to-sink systems: a basis for predicting semi-quantitative characteristics in subsurface systems. *Basin Res.* 21, 361–387. <https://doi.org/10.1111/j.1365-2117.2009.00397.x>.
- Sømme, T.O., Piper, D.J.W., Deptuck, M.E., Helland-Hansen, W., 2011. Linking onshore-offshore sediment dispersal in the golo source-to-sink system (Corsica, France) during the late quaternary. *J. Sediment. Res.* 81, 118–137. <https://doi.org/10.2110/jsr.2011.11>.
- Tan, M., Zhu, X., Liu, W., Tan, L., Shi, R., Liu, C., 2018. Sediment routing systems in the second member of the Eocene Shahejie Formation in the Liaoxi Sag, offshore Bohai Bay Basin: a synthesis from tectono-sedimentary and detrital zircon geochronological constraints. *Mar. Pet. Geol.* 94, 95–113. <https://doi.org/10.1016/j.marpetgeo.2018.04.003>.
- Thomas, S.G., Tabor, N.J., Yang, W., Myers, T.S., Yang, Y., Wang, D., 2011. Palaeosol stratigraphy across the Permian-Triassic boundary, Bogda Mountains, NW China: Implications for palaeoenvironmental transition through earth's largest mass extinction. *Palaeogeogr. Palaeoclimatol. Palaeoecol.* 308, 41–64. <https://doi.org/10.1016/j.palaeo.2010.10.037>.
- Walsh, J.P., Wiberg, P.L., Aalto, R., Nittrouer, C.A., Kuehl, S.A., 2016. Source-to-sink research: economy of the Earth's surface and its strata. *Earth-Sci. Rev.* 153, 1–6. <https://doi.org/10.1016/j.earscirev.2015.11.010>.
- Wang, J., Cao, Y., Liu, K., Liu, J., Kashif, M., 2017. Identification of sedimentary-diagenetic facies and reservoir porosity and permeability prediction: An example from the Eocene beach-bar sandstone in the Dongying Depression, China. *Mar. Pet. Geol.* 82, 69–84. <https://doi.org/10.1016/j.marpetgeo.2017.02.004>.
- Wang, J., Cao, Y.C., Wang, X.T., Liu, K.Y., Wang, Z.K., Xu, Q.S., 2018. Sedimentological constraints on the initial uplift of the West Bogda Mountains in Mid-Permian. *Sci. Rep.* 8, 1–14. <https://doi.org/10.1038/s41598-018-19856-3>.
- Wang, Jialin, Wu, C., Zhu, W., Li, Z., Wu, J., Chen, R., Wang, 2016. Tectonic-depositional environment and prototype basin evolution of the Permian-Triassic in southern Junggar Basin. *J. Palaeogeogr.* 18 (Jun), 643–660. <https://doi.org/10.7605/gdxb.2016.04.048>.
- Wang, Z., 2003. Orogeny, formation and evolution in the Bogeda Mountain Chains, Northwestern China. *Seismological Bureau of China*.
- Weaver, P.P.E., Canals, M., Trincardi, F., 2006. EUROSTRATAFORM special issue of marine geology. *Mar. Geol.* 234, 1–2. <https://doi.org/10.1016/j.margeo.2006.09.001>.
- Whittaker, A.C., Duller, R.A., Springett, J., Smithells, R.A., Whitchurch, A.L., Allen, P.A., 2011. Decoding downstream trends in stratigraphic grain size as a function of tectonic subsidence and sediment supply. *Bull. Geol. Soc. Am.* 123, 1363–1382. <https://doi.org/10.1130/B30351.1>.
- Wu, K., Zha, M., Qu, J.X., Tian, H., 2004. Control of Bogeda mountain uplift on the structural formation and evolution in Beisantai region. *J. Univ. Pet. China* 28, 1–5.
- Wu, K., Zha, M., Wang, X., Qu, J., Chen, X., 2005. Further researches on the tectonic evolution and dynamic setting of the Junggar Basin. *Acta Geosci. Sin.* 26, 217–222.
- Wu, S., 1998. Paleoclimatic discussion on Carboniferous-Permian oil-generating strata in the Northern Xinjiang. *Xinjiang Geol.* 16, 58–68.
- Wu, S., 1996. Paleoclimate of lower Permian in Xinjiang. *Xinjiang Geol.* 14, 270–277.
- Wu, X., Zhou, L., Yang, D., Qi, X., Li, B., 2012. Structure evolution and hydrocarbon accumulation the Beisantai uplift in Junggar Basin. *Chinese J. Geol.* 47, 653–668.
- Xian, B., Wang, Z., Ma, L., Zhao, C., Pu, Q., Jiang, A., Wang, J., 2017. Paleao-drainage system and integrated paleo-geomorphology restoration in depositional and erosional areas: Guantao formation in East Liaodong Area, Bohai Bay Basin China. *Earth Sci.* 42, 1922–1935.
- Xiao, H., 2015. Study on high-resolution sequence stratigraphy of the Permian in the South and East Margin of the Junggar Basin. *University of Geosciences (Beijing), China*.
- Xu, J., Snedden, J.W., Galloway, W.E., Milliken, K.T., Blum, M.D., 2017. Channel-belt scaling relationship and application to early Miocene source-to-sink systems in the Gulf of Mexico basin. *Geosphere* 13, 179–200. <https://doi.org/10.1130/GES01376.1>.
- Xu, X., Chen, C., He, X., Yu, T., Liu, Y., Liu, B., 2016. Study on sedimentary facies of Beisantai—Sha'nai oilfield in Permian Wutonggu Formation. *Xinjiang Oil Gas* 12, 6–10.
- Yang, W., Feng, Q., Liu, Y., Tabor, N., Miggins, D., Crowley, J.L., Lin, J., Thomas, S., 2010. Depositional environments and cyclo- and chronostratigraphy of uppermost Carboniferous-Lower Triassic lacustrine deposits, southern Bogda Mountains, NW China – a terrestrial fluvial paleoclimatic record of mid-latitude NE Pangea. *Glob. Planet. Change* 73, 15–113. <https://doi.org/10.1016/j.gloplacha.2010.03.008>.
- Yang, Y., 2011. Subsidence mechanisms and stratigraphic models of foreland basins. *Acta Petrol. Sin.* 27, 531–544.
- Yang, Y., Miall, A.D., 2010. Migration and stratigraphic fill of an underfilled foreland basin: Middle-Late Cenomanian Belle Fourche Formation in southern Alberta, Canada. *Sediment. Geol.* 227, 51–64. <https://doi.org/10.1016/j.sedgeo.2010.03.005>.
- Zeng, H., 2010. Stratal slicing: Benefits and challenges. *Lead. Edge (Tulsa, OK)* 29, 1040–1047. <https://doi.org/10.1190/1.3485764>.
- Zeng, H., Hentz, T.F., Wood, L.J., 2001. Stratal slicing of Miocene-Pliocene sediments in Vermilion Block 50-Tiger Shoal Area, offshore Louisiana. *Lead. Edge* 20, 408–418. <https://doi.org/10.1190/1.1438962>.
- Zhang, C., Muirhead, J.D., Wang, H., Chen, S., Liao, Y., Lu, Z., Wei, J., 2018. Lacustrine fan delta deposition alongside intrabasinal structural highs in rift basins: an example from the Early Cretaceous Jiuguan Basin, Northwestern China. *Int. J. Earth Sci.* 107, 1835–1858. <https://doi.org/10.1007/s00531-017-1575-5>.
- Zhang, L., 2011. Sedimentary Facies of Wutonggu Formation in Beisantai Area in Junggar Basin. *China University of Petroleum (East China)*.
- Zhang, X., Wang, S., Wu, X., Xu, S., Li, Z., 2016. The development of a laterally confined laboratory fan delta under sediment supply reduction. *Geomorphology* 257, 120–133. <https://doi.org/10.1016/j.geomorph.2015.12.027>.
- Zhu, H., Liu, K., Zhu, X., Jiang, Z., Zeng, H., Chen, K., 2018. Varieties of sequence stratigraphic configurations in continental basins. *Earth Sci.* 43, 770–785. <https://doi.org/10.3799/dqkx.2018.906>.
- Zhu, H., Liu, K., Zhu, X., Jiang, Z., Zeng, H., Chen, K., 2017. Advances of the source-to-sink units and coupling model research in Continental Basin. *Earth Sci.* 42. <https://doi.org/10.3799/dqkx.2017.117>.
- Zhu, H., Yang, X., Liu, K., Zhou, X., 2014. Seismic-based sediment provenance analysis in continental lacustrine rift basins: an example from the Bohai Bay Basin, China. *Am. Assoc. Pet. Geol. Bull.* 98, 1995–2018. <https://doi.org/10.1306/05081412159>.
- Zhu, H., Yang, X., Zhou, X., Li, J., Wang, D., Li, M., 2011. High resolution three-dimensional facies architecture delineation using sequence stratigraphy, seismic sedimentology: example from Dongying formation in BZ3-1 Block of western slope of Bozhong Sag, Bohai Bay Basin. *Earth Sci.* 36, 1073–1084. <https://doi.org/10.3799/dqkx.2011.113>.
- Zhu, Y., Bhattacharya, J.P., Li, W., Lapen, T.J., Jicha, B.R., Singer, B.S., 2012. Milankovitch-scale sequence stratigraphy and stepped forced regressions of the Turonian Ferron Notom Deltaic Complex, South-Central Utah, U.S.A. *J. Sediment. Res.* 82, 723–746. <https://doi.org/10.2110/jsr.2012.63>.